Diploma Thesis

Engineering Mechanics Analysis of a Moderate Fire Inside a Segment of a Subway Station

submitted in satisfaction of the requirements for the degree of
Diplom-Ingenieur
of the TU Wien, Faculty of Civil Engineering

Diplomarbeit

Ingenieurmechanische Analyse eines moderaten Feuers in einem Abschnitt einer U-Bahn-Station

ausgeführt zum Zwecke der Erlangung des akademischen Grades eines
Diplom-Ingenieurs
eingereicht an der Technischen Universität Wien, Fakultät für Bauingenieurwesen

von

Maximilian Sorgner, BSc

Matr.Nr.: 01525456

unter der Anleitung von

Univ.-Prof. Dipl.-Ing. Dr.techn. **Bernhard Pichler**

Dipl.-Ing. **Rodrigo Diaz Flores**, BSc

Institut für Mechanik der Werkstoffe und Strukturen
Technische Universität Wien
Karlsplatz 13/202, 1040 Wien, Österreich

Wien, im April 2021

Abstract

Reinforced concrete structures must be designed to withstand extreme-case scenarios such as fires. Therefore, structural engineers are interested to analyze the behavior of reinforced concrete structures subjected to a combination of mechanical loads *and* elevated temperatures. In the present thesis, a practice-oriented engineering mechanics approach is used to describe the structural behavior of a segment of a subway station subjected to regular service loads and a moderate fire. This approach combines fundamental concepts of thermo-elasto-mechanics with beam analysis software. The three-dimensional reinforced concrete structure is idealized as a frame consisting of straight beams. The rectangular columns are transformed into cylindrical beams with equivalent extensional stiffness. A series solution based on Bessel functions is newly derived, in order to the quantify the axisymmetric ingress of heat into the cylindrical columns. For all other structural elements, solutions for one-dimensional heat conduction in thickness direction are taken from the literature. The obtained temperature changes of the structural elements are translated into thermal eigenstrains. They are decomposed into three parts: an eigenstretch and an eigencurvature of the axis of the structural element, as well as an eigenwarping of its cross-sections. Corresponding decomposition rules are newly derived for *reinforced concrete* members. The derivation combines the Bernoulli-Euler hypothesis, geometric and constitutive equations of linear thermoelasticity, as well as relations between the axial force and the bending moment, on the one hand, and the axial stresses, on the other hand. The eigenstretches and eigencurvatures are *constrained* at the scale of the statically indeterminate structure. Beam analysis software is used to study the load carrying behavior of the frame structure subjected to mechanical loads as well as to thermal eigenstretches and eigencurvatures of all structural elements. The obtained axial forces and bending moments result in axial stresses which are linear across the cross-sections. The latter remain plane even under combined mechanical and thermal loading. Because of this planarity, the eigenwarping-part of the thermal eigenstrains is *prevented* at the scale of the cross-sections. This activates self-equilibrated thermal eigenstresses which are spatially nonlinear across the cross-sections. Total axial stresses are obtained from adding the thermal eigenstresses to the axial stresses quantified based on the axial forces and bending moments. The total stresses agree well with the results of a three-dimensional thermo-elastic Finite Element simulation. Thus, the engineering mechanics approach is validated. It is found that half an hour after the start of the analyzed fire, tensile stresses prevail *inside* the volume of all structural elements, in the immediate vicinities of their axes. Because the computed tensile stresses of the columns exceed the tensile strength of concrete, the engineering mechanics model is extended. A thermo-elasto-brittle approach is used to quantify load redistributions resulting from internal cracking of the columns. A significant part of the cross-sections of the columns is considered to fail due to cracking. An updated structural analysis is based on an increased value of the thermal eigenstretch of the columns and a decreased value of their extensional stiffness. These two modifications have competing effects. They lead to only insignificant redistributions of internal forces. It is concluded that tensile cracking is likely to occur unnoticed inside the columns during the fire, and that the subdivision of the developed engineering mechanics approach into a sequence of several smaller problems allows for relating causes to effects in a much more clear and insightful fashion compared to an all-in-one simulation approach such as the Finite Element Method.

Kurzfassung

Stahlbetonkonstruktionen müssen so bemessen sein, dass sie außergewöhnlichen Lastfällen wie z. B. einem Feuer widerstehen. Daher interessieren sich Bauingenieur_innen für das Verhalten von mechanisch *und* thermisch beanspruchten Stahlbetonkonstruktionen. In der vorliegenden Arbeit wird ein ingenieurmechanisches Modell entwickelt, um das Strukturverhalten eines Segments einer U-Bahn-Station unter mechanischen Gebrauchslasten und einer moderaten Feuerlast zu analysieren. Dazu werden grundlegende Konzepte der Thermoelastizität mit einer Stabstatiksoftware kombiniert. Die dreidimensionale Stahlbetonstruktur wird als dreizelliger Rahmen bestehend aus geraden Stäben idealisiert. Die rechteckigen Stützen werden in zylindrische Stäbe mit gleicher Dehnsteifigkeit transformiert. Eine Reihenlösung basierend auf Bessel Funktionen wird hergeleitet, um den axialsymmetrischen Wärmeeintritt in die zylindrischen Säulen zu quantifizieren. Für die anderen Strukturelemente werden Lösungen für eindimensionale Wärmeleitung in Dickenrichtung aus der Literatur entnommen. Die berechneten Temperaturänderungen der Strukturelemente werden in thermische Eigendehnungen übersetzt und in drei Teile zerlegt: eine Eigenstreckung und eine Eigenkrümmung der Achse der Strukturelemente sowie eine Eigenverwölbung der Querschnitte. Entsprechende Regeln für diese Aufteilung werden für *Stahlbeton*-Elemente hergeleitet, wobei die Annahme vom Ebenbleiben der Querschnitte, geometrische und konstitutive Gleichungen der linearen Thermoelastizitätstheorie sowie die Beziehungen zwischen der Normalkraft bzw. dem Biegemoment und den axialen Normalspannungen eingehen. Die Eigenstreckungen und Eigenkrümmungen sind auf der Skala der statisch unbestimmten Struktur *behindert*. Mit einer Stabstatiksoftware wird das Tragverhalten des Rahmens unter mechanischen Belastungen sowie thermischen Eigenstreckungen und Eigenkrümmungen untersucht. Die berechneten Normalkräfte und Biegemomente führen zu axialen Normalspannungen, die über die Querschnitte linear verlaufen. Letztere bleiben auch unter kombinierter mechanischer und thermischer Belastung eben. Daher ist der Eigenverwölbungsanteil der thermischen Eigendehnungen auf der Skala der Querschnitte *verhindert*. Dies aktiviert thermische Eigenspannungen, die über die Querschnitte nichtlinear verlaufen und eine Gleichgewichtsgruppe darstellen. Die axialen Gesamtspannungen ergeben sich als Summe der thermischen Eigenspannungen und der Normalspannungen zufolge Normalkraft und Biegemoment. Die Gesamtspannungen stimmen gut mit den Ergebnissen einer dreidimensionalen thermoelastischen Finite Elemente Simulation überein. Somit ist das ingenieurmechanische Modell validiert. Die Berechnungsergebnisse verdeutlichen, dass eine halbe Stunde nach Beginn des analysierten Feuers Zugspannungen im Volumen aller Strukturelemente auftreten. Da die berechneten Zugspannungen der Stützen die Zugfestigkeit von Beton überschreiten, wird das ingenieurmechanische Modell erweitert. Es werden jene Lastumverteilungen quantifiziert, die sich aus sprödem Zugrisswachstum in Inneren der Säulen ergeben. Dabei wird berücksichtigt, dass wesentliche Teile der Querschnitte der Säulen versagen. Eine aktualisierte Strukturanalyse basiert auf einem erhöhten Wert der thermischen Eigenstreckung der Säulen und einem verringerten Wert ihrer Dehnsteifigkeit. Diese beiden Modifikationen haben entgegenwirkende Effekte. Sie führen zu nur unbedeutenden Lastumverteilungen. Somit wird der Schluss gezogen, dass Zugrisse in den Säulen während des Brandes wahrscheinlich unbemerkt auftreten. Das entwickelte ingenieurmechanische Modell ermöglicht es aufgrund seiner Gliederung in mehrere kleinere Probleme, Ursachen und Effekten viel klarer und aufschlussreicher in Beziehung zu setzen als das mit einem einstufigen Simulationsansatz wie der Finite Elemente Methode möglich ist.

Danksagung

An dieser Stelle möchte ich mich bei all denjenigen bedanken, die mich beim Verfassen der vorliegenden Diplomarbeit und während meines Studiums unterstützt haben. Allen voran bedanke ich mich bei Herrn Univ. Prof. Dipl.-Ing. Dr. techn. Bernhard Pichler für die Hauptbetreuung der Arbeit, die zahlreichen fachlichen Diskussionen sowie die wertvolle sprachliche und inhaltliche Unterstützung. Ebenso möchte ich mich bei Herrn Dipl.-Ing. Rodrigo Diaz Flores für die Unterstützung im Umgang mit Abaqus und der Überprüfung der Daten, für die kontinuierliche Begleitung sowie den sprachlichen und fachlichen Input bedanken. Auch meiner Kollegin Sophie möchte ich Dank für ihren Beistand und die motivierenden Worte in der „heißen“ Phase der Diplomarbeit aussprechen. Ein besonderer Dank gebührt meinen Eltern, Martin und Gerda, die mich Zeit meines Lebens unterstützt und gefördert haben, mir zu jeder Zeit mit Rat und Tat zur Seite gestanden sind, und mir das Studium an der TU Wien ermöglicht haben. Ich möchte mich auch bei meiner Schwester Johanna, meinem Schwager Markus und meinem Taufkind Valentina für ihre Unterstützung bedanken. Insbesondere danke ich Valentina für die ruhigen Stunden während ich an der Diplomarbeit gearbeitet habe und den nötigen Ausgleich in den Pausen, die ich sehr gerne mit ihr verbracht habe. Abschließend möchte ich mich bei meinen Freunden bedanken. Dabei möchte ich meinem Studienkollegen Thomas, der mich durch das gesamte Studium begleitet und mich in weniger motivierten Zeiten immer wieder angespornt hat, besonderen Dank aussprechen.

Contents

Chapter 1

Introduction

Reinforced concrete is the most commonly used and one of the most widely investigated construction materials in the world. Structural engineers are interested in the load-carrying behavior of reinforced concrete structures. The development of appropriate models that reliably and efficiently predict their behavior when subjected to a combination of elevated temperatures and mechanical loads, however, remains a challenge.

Investigations in this area can be separated into two main fields of research, which are very often found in combination with each other: experimental investigations based on large-scale tests, and numerical simulations involving either the full complexity of a full-scale test, or a simplified, practice-oriented analysis of specific elements of a structure. As regards experimental campaigns, Vecchio and Sato performed three large scale tests to reinforced concrete frames subjected to a combination of mechanical loads and controlled thermal loads specified at the inner surface of the frame [30]. Ring et al. performed a large-scale fire test on an underground concrete frame structure [23], the results of which were used for the elaboration and validation of numerical Finite Element simulations [24]. Kamath et al. conducted a full-scale fire test on a reinforced concrete frame, which was first subjected to simulated seismic damage to investigate the material behavior of reinforced concrete due to fire following an earthquake [19]. Recently, Lu et al. performed a large-scale fire test on a segment of a subway station [21].

Regarding purely numerical simulations, thermo-mechanical three-dimensional Finite Element (FE) simulations have been performed on reinforced concrete beams [1, 15, 22, 26, 32], and columns [3, 32] subjected to elevated temperatures. Diaz et al. modeled, by means of three-dimensional FE simulations, the structural behavior of an underground frame structure subjected to the first 30 minutes of the fire test presented in [21], representative of a moderate fire scenario [7]. Simplified methods have also been developed in order to optimize the computational power required by complex FE simulations that attempt to reproduce fire scenarios. In this context, simple numerical models have been developed to analyze the response of reinforced concrete frames [29], the resistance of reinforced beams [4, 9, 20], and of cylindrical columns [14], even using "transformed" cross-sections in order to analyze and design reinforced concrete columns as a cross-section with uniform material properties [5, 28]. El-Fitiany and Youssef presented a simplified method to calculate internal compression forces and corresponding moments for heated concrete structures that can be easily applied using available commercial linear structural analysis software to predict the fire performance of reinforced concrete structures [10–13]. El-Tayeb et al. gave a more intuitive insight into the effect of thermal loads on reinforced concrete structures by separating the temperature distribution into a uniform, a linear and a non-linear contribution, and described the importance of the non-linear part, exclusive of transient thermal conditions [27]. Wang et al. further advanced this method by introducing a semi-analytical solution which determines the non-linear thermal stresses developed by concrete pavements due by temperature changes on the top surface in transient thermal conditions [31]. This approach was specialized for slender beams with homogeneous material behavior [2, 17]. Finally, Schmid then extended

this solution for concrete pavements with temperature changes on both, the top and bottom surface [25].

The present study attempts to describe the structural behavior of the segment of a subway station presented in [7, 21] subjected to a moderate fire scenario, as described in [7], by means of an inexpensive, practice-oriented model that combines the use of inexpensive beam models and thermo-elasto-mechanics fundamentals. This simulation is organized in five steps. The first one refers to the idealization of the originally three-dimensional structure into a frame structure with one-dimensional beam elements, where the Euler-Bernoulli beam theory is applicable. In order to consider the reinforcement of the structure and its mechanical properties, the initially non-uniform cross section is transformed into an equivalent cross-section with uniform properties. The second step refers to the solution of the transient heat conduction problem. Semi-analytical solutions to the one-dimensional heat conduction problems are used in order to predict the temperature field inside the whole reinforced concrete structure. Notably, the transformation of initially rectangular columns into equivalent cylindrical ones exhibiting the same extensional stiffness allows for a prediction of the temperature field inside the columns to be made based on an axisymmetric temperature problem that can be solved semi-analytically. The third step refers to the quantification of the thermal stress contributions, based on a thermo-elasto-mechanics analysis and the semi-analytical solutions of the heat conduction problems. Herein, it must be determined whether the eigenstrains developed by each cross-section are free to develop, constrained, or prevented. This is determined partly at the larger, structural level, and partly at the smaller, cross-sectional level. At the structural level, thermal stresses occur due to the constraints imposed by the boundary conditions of the structure onto the development of the thermal eigenstretch and eigencurvature. At the cross-sectional level, thermal stresses develop due to the Euler-Bernoulli assumption that plane sections remain plane, which thus prevents the development of a spatially nonlinear, self-equilibrated eigenwarping of the cross-section. The fourth step refers to the use of the beam analysis software RStab [8] in order to predict the internal forces resulting by the combination of the mechanical loading that represents the service conditions of the structure, and the thermal loading resulting from the moderate fire. The fifth and last step refers to the superposition of the stresses resulting from both load cases and the self-equilibrated, nonlinear part of the thermal stresses, resulting from prevented eigenwarping of the cross-section.

The present master thesis is organized as follows. Chapter 2 refers to the prerequisites for this study, including a brief description and essential results of the scaled fire test and the FE simulation of the reinforced concrete structure as documented in [7]. Chapter 3 refers to the engineering mechanics analysis pushed forward in this thesis. In Chapter 4, the results of the engineering mechanics analysis are compared with those from the FE simulation. The thermo-elastic mode analysis is extended to an thermo-elasto-brittle mode, accounting for tensile cracking of concrete in the core regions of the columns. Chapter 5 contains the summary and the conclusions drawn from the present study.

Chapter 2

Prerequisites for the present study

2.1 Results from a scaled fire test

A scaled fire test was performed [21] on a structure inspired by the upper floor of a three-span, two-floor reinforced concrete frame, commonly used in underground stations in China. The motivation to perform the test, was to identify the temperature at the inner surface as well as the temperature histories and strains inside the structure. The tested structure was placed sidelong on top of a furnace and closed with a fire-resistant cover. A frame of steel with hydraulic presses and supports was located around the model to simulate service conditions, see Fig. 2.1. The

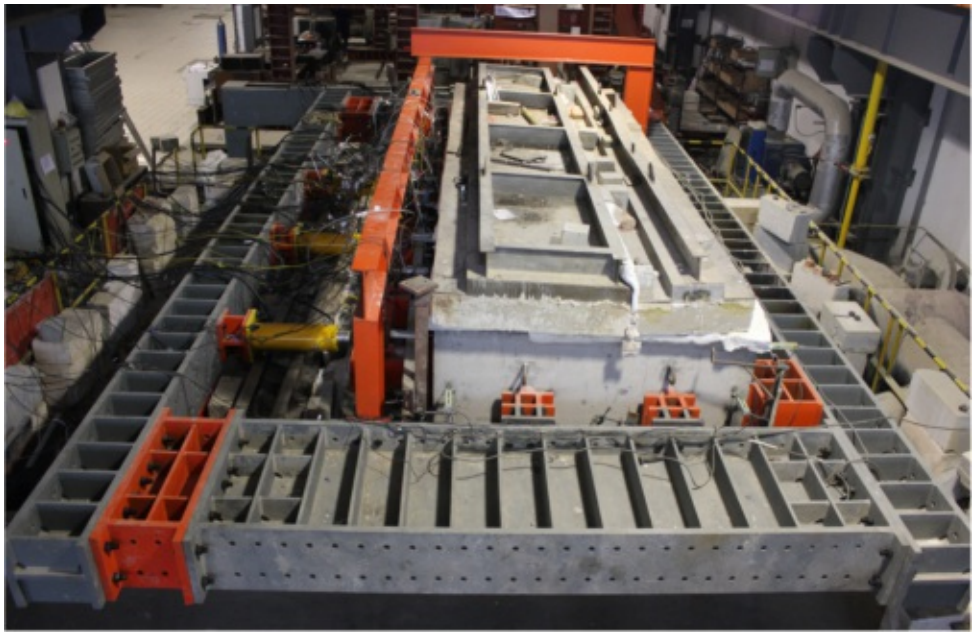

Fig. 2.1: Setup of the large-scale fire test [7, 21].

real structure described in [7] was tested at a scale of 1:4 with a width of 5260 mm, a height of 1880 mm, and an axial length of 1200 mm, see Fig. 2.2a. Because of the distance between neighboring columns in axial direction, the cross-section of the columns of the tested structure were scaled by 1:5, see [7] for details. The cross-section of the columns for the scaled fire test are illustrated in Fig. 2.2a. The reinforcement of each element of the structure was scaled by using the same reinforcement ratio as the structure at real scale. This leads to the reinforcement drawing of the tested structure [7], see Fig. 2.2b. The structure was produced with normal concrete "C40", with a mass density of 2373 kg/m^3 and a concrete cover of 30 mm. Before the concrete was cast, the temperature and strain sensors at the slabs and walls were installed. At the top slab in the right cell and the right wall, temperature sensors were located at minimum

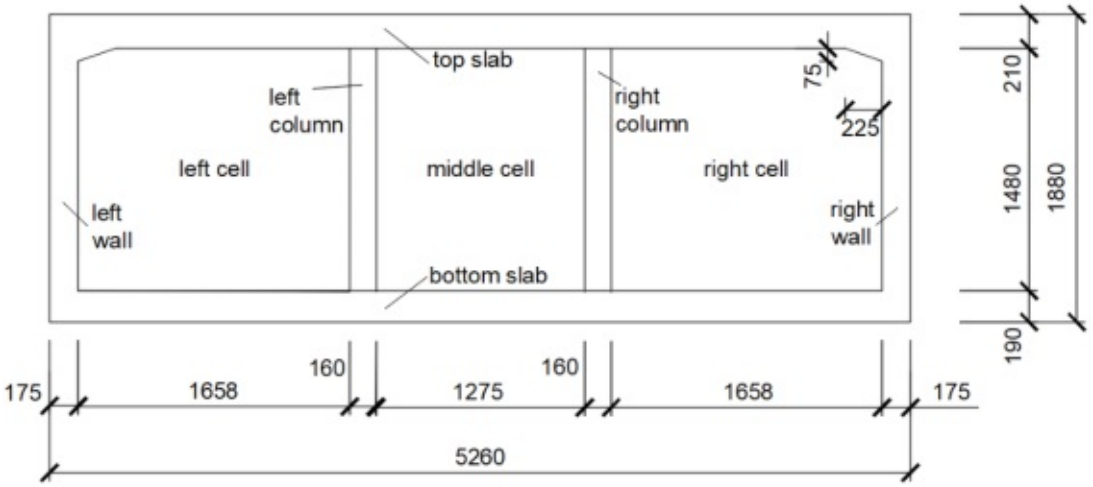

(a)

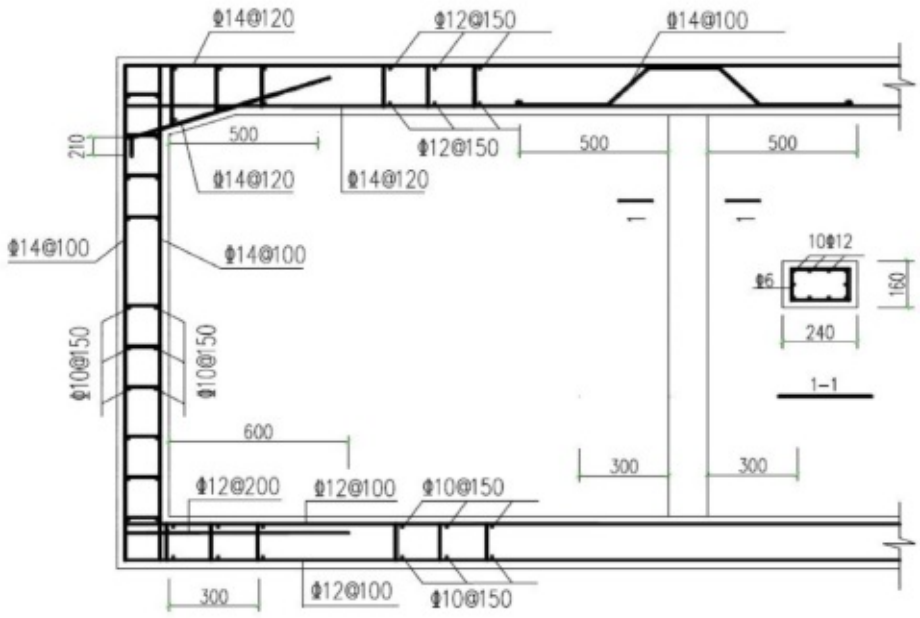

(b)

Fig. 2.2: **(a)** Geometric dimensions of the tested structure, and **(b)** reinforcement drawing.

cover depth amounted to 2 mm only. During the first 1800 s of heating the inner surface, the temperature of the outer surface was constant. The temperature sensors recorded entries at intervals of 20 s. Thus, the first 1800 s of the fire test were documented by 90 readings of each sensor.

2.2 Results from Finite Element simulations

Based on the scaled fire test, the structure was simulated by means of three-dimensional, non-stationary Finite Element (FE) simulations using the commercial software Abaqus FEA 2016. The mesh consisted of 139,040 linear hexahedral brick finite elements, with eight nodes and one

temperature degree of freedom per node, see Fig. 2.3. These elements are referred to as "DC3D8" by ABAQUS CAE [6]. The characteristic size of the finite elements amounted to 30 mm [7]. Fig. 2.4 illustrates the idealized geometric boundary conditions and their locations as well as the

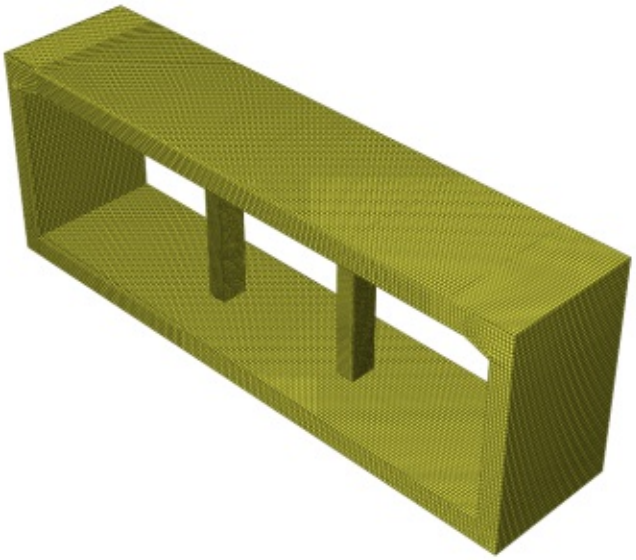

Fig. 2.3: Three-dimensional FE mesh of the analyzed structure [7].

locations of the point loads P_1, P_2, and P_3, that represent the hydraulic presses. The magnitudes of the point loads are presented in Table 2.1. Because of the definition of the stiffness matrices of FE, point loads are idealized as surface stresses with high intensity and small finite area. Given

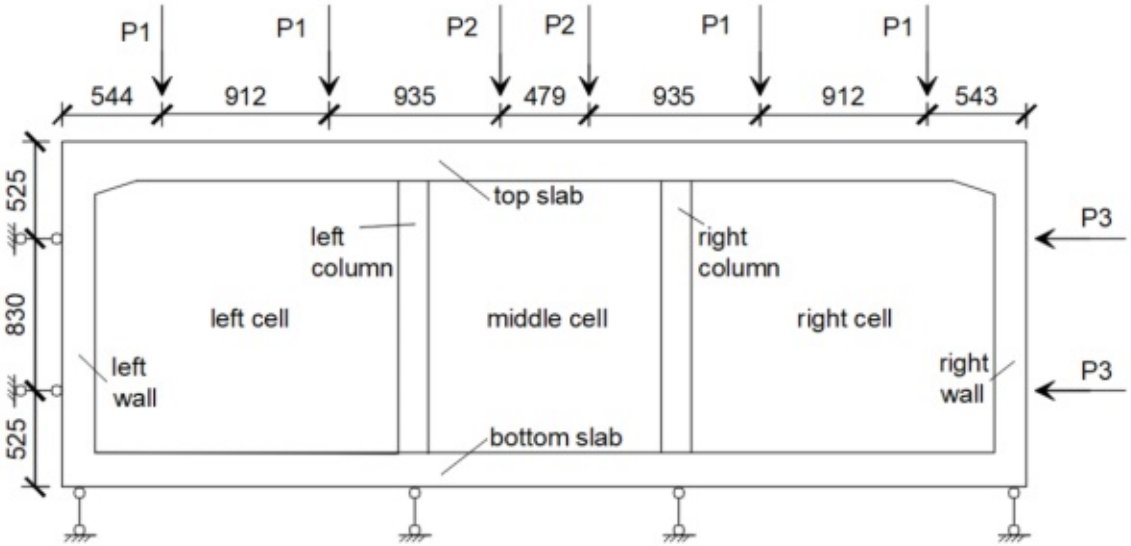

Fig. 2.4: Support and loading conditions of the tested structure [7].

that the thermal properties of the tested structure were unknown, the values of the specific heat capacity and the thermal conductivity were estimated in accordance with building codes and scientific studies, see Table 2.2. According to the insights in [7], the temperature change at the steel bars may be assumed to be equal to that of the concrete at its immediate vicinity. Thus, this thermal simulation of the structure depends on the thermal properties of concrete only. For

Tab. 2.1: Intensities of the point loads imposed on the structure in order to simulate service conditions [7].

	P_1	P_2	P_3
Loadings [kN]	192.0	151.2	120.0

Tab. 2.2: Thermal properties of concrete [7].

Property	**Value**
Specific heat capacity [J/kgK]	900
Thermal conductivity [W/mK]	1.6

the thermo-mechanical analysis, the steel needs to be taken into account. The reinforcement were modeled as one-dimensional truss elements. The values of specific properties of concrete and steel, defined in [7], were assigned to the corresponding elements, see Table 2.3. In order to limit the complexity of the model, the reinforcement were overlain to the concrete. The properties in Table 2.3 are representative for elastic material behavior at room temperature. For simulation of

Tab. 2.3: Mechanical properties of concrete and steel [7].

Property	**concrete**	**steel**
Modulus of elasticity [GPa]	33.4	195
Poisson's ratio [-]	0.2	0.3
Thermal expansion coefficient [$^\circ C^{-1}$]	9.03×10^{-6}	12.2×10^{-6}

non-stationary heat conduction with ABAQUS CAE [6] the temperature data of the scaled fire test described in Section 2.1 and [7] was used to approximate the temperature histories at the inner surface of the top slab and the right wall in a first step of the analysis. At the columns there was a temperature sensor at the middle of the cross-section only. Thus, the temperature evolution at the outer surface of the columns was simulated by fitting the prescribed temperature histories of the top slab; for detail see [7]. In addition to the location of the measurements near the surface, the structure was subdivided into three sub-regions with piecewise uniform temperature histories:

1. The slabs were subjected to the temperature history, measured at the midspan of the right cell of the top slab, at depth of 2 mm from the inner surface, see Fig 2.5a.

2. The walls were subjected to the temperature history, measured at the midspan of the right cell of the top slab, at depth of 2 mm from the inner surface, see Fig. 2.5b.

3. The columns were subjected to the temperature history, measured at the midspan of the right cell of the top slab, at depth of 2 mm from the inner surface, scaled by a fitting-factor, see Fig. 2.5c.

This temperature histories were used to simulate the boundary conditions of heat conduction for the FE analysis with ABAQUS CAE [6], documented in [7].

The thermo-mechanical results of the FE simulation were evaluated at selected sections of the structure, representing the stress component σ_{xx} of Cauchy's stress tensor at the mid-plane in

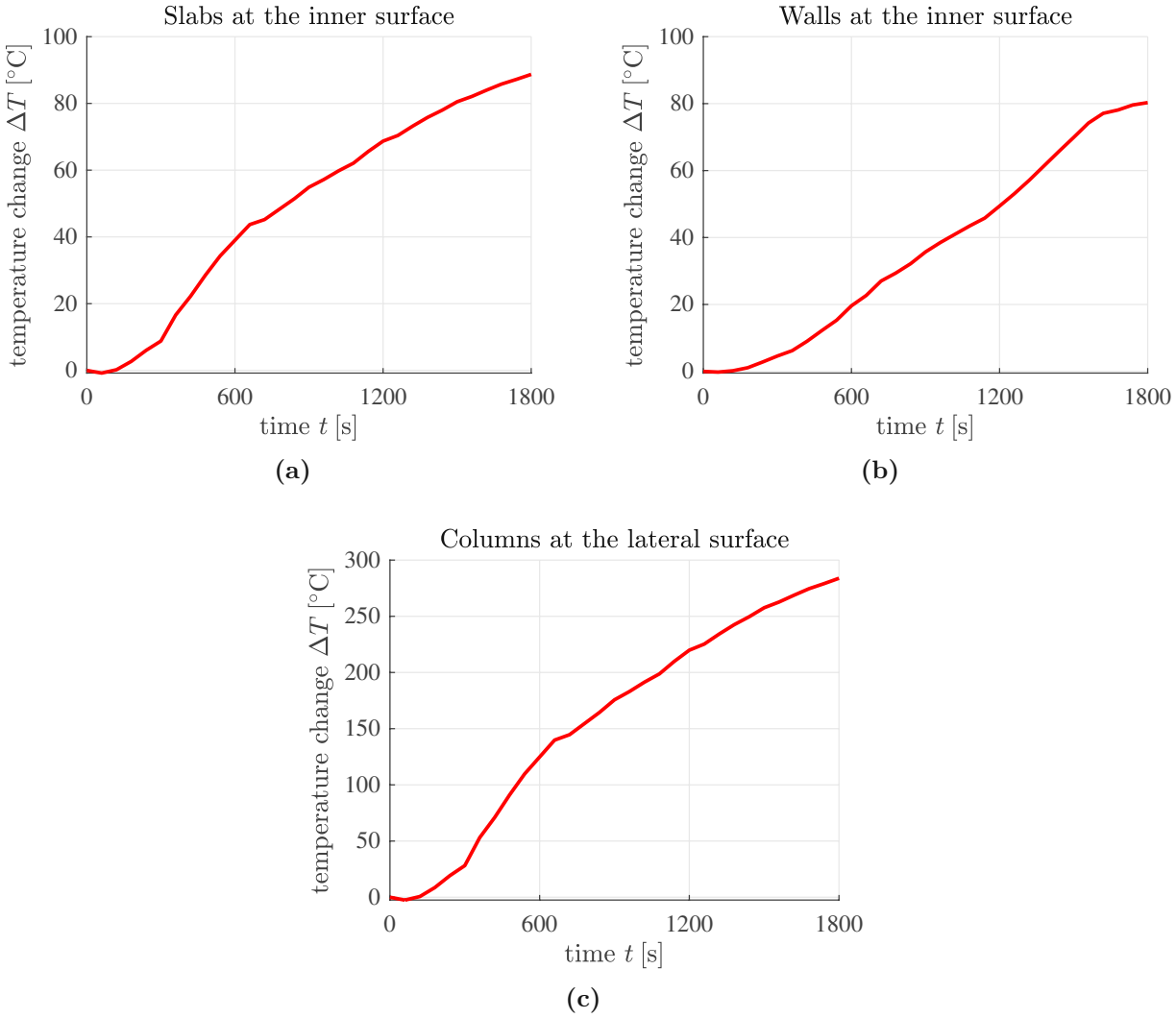

Fig. 2.5: Temporal evolution of temperature changes at the surfaces of the structural elements, discretized in 90 readings: **(a)** slabs, **(b)** walls, and **(c)** columns.

axial direction. The linear shape-functions of the chosen elements yield element-wise constant stresses. In Chapter 4 the described stress distributions of the FE simulation are illustrated as dashed lines, see Figs. 4.7 - 4.18.

Chapter 3

Engineering mechanics analysis

In the following, a simplified engineering mechanics analysis of the scaled fire test described in Chapter 2 is performed using a beam analysis software under the assumption of the first-order beam theory. The results are then compared with the ones obtained from three-dimensional FE simulations. For this analysis, all structural elements are idealized as beams. Thus, the slabs and walls of the structure will be simulated as prismatic beams. Because of the geometry of the plates and the constant temperature at the outer surface, the generally three-dimensional heat conduction problem may be approximated as a one-dimensional heat conduction in thickness direction. The prismatic columns, located in the mid-plane of the structure, are thermally loaded on all four lateral surfaces. To reduce the two-dimensional heat conduction problem to a one-dimensional one, the prismatic columns will be transformed into cylindrical ones. This provides the motivation for solving both, one-dimensional heat conduction in thickness direction of prismatic beams and radial heat conduction in axisymmetric cylindrical columns. The prismatic beams are defined as structures with doubly-symmetric cross-sections in a Cartesian coordinate system with origin at the axis of the beam. The cylindrical columns are defined as structures with axisymmetric cross-sections. In order to consider the reinforcement of concrete, a non-uniform modulus of elasticity $E(y,z)$ and thermal expansion coefficient $\alpha_T(y,z)$ are considered at a cross-sectional scale in Section 3.2. They are represented as equivalent "transformed" cross-section. Axial stresses result from the mechanical loading, from the boundary-conditions-dependent constraint of the thermal eigenstretch and eigencurvature of the axis of the beam, and from the thermal eigenwarping of the cross-section of the beam, which is prevented at a cross-sectional level as a consequence of the assumption that plane sections remain plane. The total stresses then are calculated as a superposition of these cases. In Section 3.3 the simulation with beam analysis software at structural scale will be performed. The results of the thermo-elasto-mechanics are discussed in Chapter 4.

3.1 Semi-analytic solutions of the heat conduction problem

The general form of the heat equation for the case of a three-dimensional heat conduction problem is given as [18]

$$\rho\, c\, \dot{T} - \nabla \cdot (\boldsymbol{K} \cdot \nabla T) = 0\,, \tag{3.1}$$

where ρ is the mass density, c is the specific heat capacity, $\boldsymbol{K}$ is the second order tensor of thermal conductivity, ∇ is the nabla operator. The thermal conductivity in the case of isotropic heat conduction properties is defined as $\boldsymbol{K} = K \cdot \boldsymbol{I}$ with the second order identity tensor defined as $\boldsymbol{I} = \sum_{i=1}^{3} \underline{e}_i \otimes \underline{e}_i$. Thus, the heat conduction problem in Eq. (3.1) reads as

$$\dot{T} - a\, \nabla \cdot (\boldsymbol{I} \cdot \nabla T) = 0 \qquad \text{with} \qquad a = \frac{K}{\rho c}\,, \tag{3.2}$$

where a denotes the thermal diffusivity. The partial differential equation (3.2) will be solved for one-dimensional heat conduction in thickness direction of prismatic beams and radial heat conduction of cylindrical columns with time-dependent boundary conditions at the surfaces according to the temperature histories, see Fig. 2.5. At the beginning, the temperature at the surface is equal to a reference temperature T_{ref}. This yields a constant initial condition for solving the heat conduction problem. Because of the linearity of the partial differential equation (3.2), the superposition principle applies and the time-dependent boundary conditions in temperature can be discretized in N temperature increments ΔT_k with time-independent boundary conditions at the surfaces, where $k = 1, 2, ..., N_T$, see Fig. 3.1. This can be used to create elementary solutions at each temperature increment ΔT_k that can be superimposed to a semi-analytical solution for the given boundary conditions. In this context, the temperature increments are defined as:

$$T(t_0) = T_{ref} \qquad \text{initial condition,} \tag{3.3}$$

$$\Delta T_k = T(t_k) - T(t_{k-1}) \qquad \text{constant boundary condition at the surface for one time increment.} \tag{3.4}$$

where t_k is the time of the next temperature increment and t_{k-1} the time of the increment before. The difference between t_k and t_{k-1} of Eq. (3.4) is the time step between the temperature measurements of the tested structure, see Fig. 3.1.

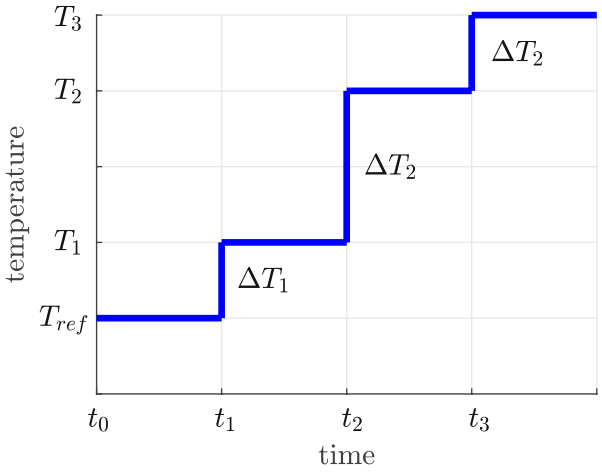

Fig. 3.1: Thermal boundary conditions of the structural elements: approximation of a continuous temperature evolution in a step-wise fashion [17, 31].

3.1.1 One-dimensional heat conduction in thickness direction of prismatic beams

Specification of the heat equation (3.2) for a Cartesian coordinate system and one-dimensional heat conduction in thickness direction z with temperature $T = T(z, t)$ and thermal diffusivity a, yields:

$$\frac{\partial T}{\partial t} - a\frac{\partial^2 T}{\partial z^2} = 0\,. \tag{3.5}$$

At the beginning ($t = 0$) the temperature of the prismatic beam is equal to the reference temperature T_{ref}. On each time step t_k with $k = 1, 2, ...N_T$, where N_T is the total number of temperature increments, the temperature of the bottom surface of the beam T^{bot} is constant and depends on the temperature histories as presented in Fig. 2.5a and 2.5b. It is assumed that the

heat flux across the lateral surfaces is equal to zero and the one-dimensional heat equation (3.5) is applicable. The temperature of the top surface is equal to T_{ref}. In this case the initial condition and the boundary conditions can be written as:

$$T(z, t = 0) = T_{ref} \qquad \text{initial condition,} \tag{3.6}$$

$$\left.\begin{aligned} T(z = -\tfrac{h}{2}, t) &= T_{ref} \\ T(z = +\tfrac{h}{2}, t) &= T^{bot}(t) \end{aligned}\right\} \text{boundary conditions.} \tag{3.7}$$

The solution of the one-dimensional heat equation (3.5) for one temperature increment prescribed on the top surface ΔT^{top} and constant temperature at the bottom surface of the structure is documented in the literature, e.g., [2]. Reversing the positive direction of the z axis and inserting ΔT^{bot} instead of ΔT^{top} in the solution [2, 31] yields the distribution of the temperature for one temperature increment prescribed on the bottom surface. Summation of the elementary solutions of N temperature increments on the bottom surface of prismatic beams reads as

$$\begin{aligned} \Delta T(z,t) = &\sum_{k=1}^{N_T} \Delta T_k^{bot} \left(\frac{1}{2} + \frac{z}{h}\right) \\ &+ \sum_{n=1}^{\infty} \exp\left(-\frac{(2n-1)^2\pi^2 a\langle t - t_k\rangle}{h^2}\right)\left[\frac{2\Delta T_k^{bot}(-1)^n}{(2n-1)\pi}\cos\left(-(2n-1)\pi\frac{z}{h}\right)\right] \\ &- \sum_{n=1}^{\infty} \exp\left(-\frac{(2n\pi)^2 a\langle t - t_k\rangle}{h^2}\right)\left[\frac{\Delta T_k^{bot}(-1)^n}{n\pi}\sin\left(-2n\pi\frac{z}{h}\right)\right], \end{aligned} \tag{3.8}$$

where h is the height of the cross-section and the angled brackets denote the Macaulay operator:

$$\langle t - t_k\rangle := \frac{1}{2}\left(t - t_k + |t - t_k|\right). \tag{3.9}$$

In Eq. (3.8), the temperature difference ΔT_k^{bot} denotes the boundary condition at temperature increment k, see Fig. 3.1 and Eq. (3.4).

3.1.2 Radial heat conduction in axisymmetric cylindrical columns

Specification of the heat equation (3.2) for a cylindrical coordinate system with spatially uniform boundary conditions at the lateral surface delivers an axisymmetric heat conduction problem where the temperature $T = T(r, t)$, yielding a partial differential equation with variable coefficients, also known as Bessel differential equation [16], which reads as

$$\frac{\partial T}{\partial t} - a\left(\frac{\partial^2 T}{\partial r^2} + \frac{1}{r}\frac{\partial T}{\partial r}\right) = 0\,. \tag{3.10}$$

At the beginning ($t = 0$), the temperature of the cylindrical column is equal to the reference temperature T_{ref}. On each time step t_k with $k = 1, 2, ...N_T$, where N_T is the total number of temperature steps, the temperature of the lateral surface of the column T^{lat} is constant (Fig. 3.1)

and depends on the temperature history as presented in Fig. 2.5c. In this case, the initial condition and the boundary condition can be written as:

$$T(r, t = 0) = T_{ref} \qquad \text{initial condition,} \tag{3.11}$$

$$T(r = R, t) = T^{lat}(t) \qquad \text{boundary condition.} \tag{3.12}$$

The solution of the radial heat conduction problem in Eq. (3.10) for one temperature increment prescribed on the lateral surface ΔT_k^{lat} of the structure as defined in Eq. (3.4) is documented in Appendix A. Summation of the elementary solutions of N_T temperature increments on the lateral surface of cylindrical columns and subtracting the reference temperature T_{ref} reads as

$$\Delta T(r, t) = \Delta T^{lat} + \sum_{k=1}^{N_T} \frac{2(T_{ref} - \Delta T_k^{lat})}{R} \sum_{n=1}^{\infty} \frac{J_0(\lambda_n r)}{J_1(\lambda_n R)\lambda_n} \exp(-\lambda_n^2 a \langle t - t_k \rangle) \,, \tag{3.13}$$

where ΔT^{lat} denotes the total temperature change on the lateral surface, defined as the summation of all temperature increments ΔT_k^{lat} in Eq. (3.4). J_0 and J_1 denote the Bessel functions of the first kind with their eigenvalues λ_n, R denotes the radius of the column and the angled brackets denote the Macauley operator defined in Eq. (3.9).

3.2 Engineering Mechanics modeling at cross-sectional scale

3.2.1 Engineering thermo-elasto-mechanics of reinforced concrete beams

The thermal eigenstrains, ε^e, developed at the points y and z inside the cross-section of a beam, see Fig. 3.2, are equal to the thermal expansion coefficient evaluated at those points, $\alpha_T = \alpha_T(y, z)$, multiplied with the change of temperature, measured relative to the reference configuration, $\Delta T(z, t) = T(z, t) - T_{ref}$, as

$$\varepsilon_{xx}^e = \varepsilon_{yy}^e = \varepsilon_{zz}^e = \alpha_T \Delta T \,. \tag{3.14}$$

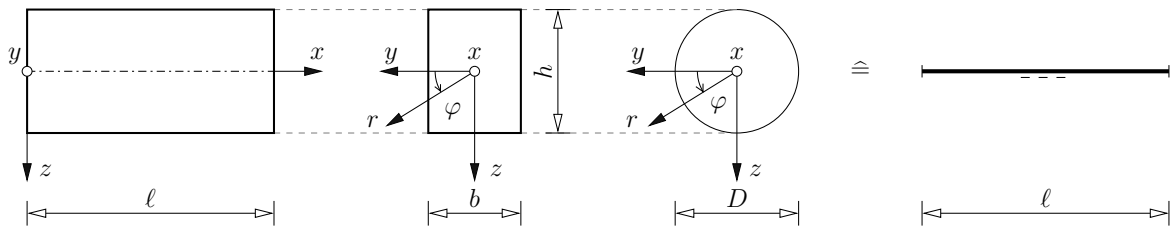

Fig. 3.2: Local coordinate systems describing positions inside and at the boundary of the structural elements: x denotes the longitudinal axis; y and z denote Cartesian coordinates of the cross-section; r and φ denote cylindrical coordinates.

In a transient heat conduction problem, the thermal eigenstrains are spatially nonlinear along the thickness direction, see e.g., [17, 25, 31]. When it comes to the quantification of thermal stresses, the question must be answered whether the eigenstrains are free to develop, constrained, or prevented. This question is answered partly at the larger, structural level, and partly at the smaller, cross-sectional level. To this end, the spatially nonlinear eigenstrains are subdivided into three parts. They refer to an eigenstretch of the beam, an eigencurvature of the beam, and an eigenwarping of the cross-section. The eigenstretch and the eigencurvature of the axis of the

beam cause axial stresses depending on the boundary conditions that constrain the deformation of the structure. On the other hand, the assumption that plane sections remain plane means that the eigenwarping of the cross-section of the beam is prevented, thus always resulting in nonlinear thermal stresses. Herein, we focus on doubly-symmetric cross-sections with non-uniform modulus of elasticity and thermal expansion coefficient, $E(y,z)$ and $\alpha_T(y,z)$, respectively, assuming a coordinate system with origin at the axis of the beam, see Fig. 3.2. This yields

$$\int_A E\, z \, \mathrm{d}A = 0\,. \tag{3.15}$$

The first step refers to the kinematics of the Euler-Bernoulli theory for slender beams:

$$u = u_0 - \frac{\partial w_0}{\partial x}\, z\,, \tag{3.16}$$

where u denotes the displacement components in x-direction, at any point within the volume of the beam. u_0 and w_0 denote the displacement components at the axis of the beam. Eq. (3.16) essentially describes that cross-sections remain plane and normal to the deformed axis of the beam, also in the deformed configuration (= Euler-Bernoulli hypothesis).

The second step refers to ("total") axial strain component ε_{xx} of the linearized strain tensor. It is defined as

$$\varepsilon_{xx} = \frac{\partial u}{\partial x}\,. \tag{3.17}$$

Inserting Eq. (3.16) into Eq. (3.17) yields

$$\varepsilon_{xx} = \frac{\partial u_0}{\partial x} - \frac{\partial^2 w_0}{\partial x^2}\, z\,. \tag{3.18}$$

Eq. (3.18) is usually reformulated in terms of the stretch of the axis of the beam, $\varepsilon_0 = \partial u_0/\partial x$, and its curvature, $\kappa_0 = -\partial^2 w_0/\partial x^2$. This yields

$$\varepsilon_{xx} = \varepsilon_0 + \kappa_0\, z\,. \tag{3.19}$$

The third step refers to axial stress component σ_{xx} of Cauchy's stress tensor. In thermoelasticity, it reads as

$$\sigma_{xx} = E\,(\varepsilon_{xx} - \varepsilon^e_{xx})\,. \tag{3.20}$$

Inserting Eqs. (3.14) and (3.19) into (3.20) yields

$$\sigma_{xx} = E\,(\varepsilon_0 + \kappa_0\, z - \alpha_T \Delta T)\,, \tag{3.21}$$

where the modulus of elasticity is a function of the y- and z-coordinates which describe points inside the cross-sections of the beam, i.e. $E = E(y,z)$.

The fourth step refers to axial force N. It is energetically conjugate to the displacements u_0 and read as

$$N = \int_A \sigma_{xx} \, \mathrm{d}A\,. \tag{3.22}$$

Inserting Eq. (3.21) into (3.22) yields under consideration of (3.15):

$$\begin{aligned} N &= \int_A E\left(\varepsilon_0 + \kappa_0\, z - \alpha_T \Delta T\right)\, \mathrm{d}A\,, \\ &= \underbrace{\int_A E\, \mathrm{d}A}_{\overline{EA}}\, \varepsilon_0 - \underbrace{\int_A E\, \alpha_T \Delta T\, \mathrm{d}A}_{\overline{EA}\,\varepsilon_0^e}\,, \\ &= \overline{EA}(\varepsilon_0 - \varepsilon_0^e)\,. \end{aligned} \tag{3.23}$$

Eq. (3.23) is the motivation to introduce the effective extensional stiffness of the beam as

$$\overline{EA} = \int_A E\, \mathrm{d}A\,. \tag{3.24}$$

In the case of a reinforced concrete beam, $\overline{EA}$ can be rewritten as

$$\begin{aligned} \int_A E\, \mathrm{d}A &= \int_{A_c} E_c\, \mathrm{d}A + \int_{A_s} E_s\, \mathrm{d}A\,, \\ &= E_c A_c + E_c \underbrace{\frac{E_s}{E_c}}_{n_E} \sum_{j=1}^{L} A_{s,j}\,, \\ &= E_c \underbrace{\left[A_c + n_E \sum_{j=1}^{L} A_{s,j}\right]}_{A_{tr}}\,, \end{aligned} \tag{3.25}$$

where n_E refers to the ratio between the modulus of elasticity of steel, E_s, and concrete, E_c, j refers to each one of the L individual reinforcement bars existing within the cross-section, and $A_{tr} = A_c + n_E \sum_{j=1}^{L} A_{s,j}$ refers to the total area of the "transformed" section with A_c denotes the area of concrete and A_s denotes the area of steel. Thus, one can conclude from Eq. (3.23) that the eigenstretch of the axis of the beam is calculated as

$$\varepsilon_0^e = \frac{1}{\overline{EA}} \int_A E\, \alpha_T \Delta T\, \mathrm{d}A\,, \tag{3.26}$$

which in case of a concrete beam that presents a constant temperature in each reinforcement bar, considering Eqs. (3.24) and (3.25), leads to

$$\begin{aligned}\varepsilon_0^e &= \frac{1}{\overline{EA}}\left[\int_{A_c} E_c\,\alpha_{T,c}\,\Delta T\;\mathrm{d}A + \sum_{j=1}^{L} E_s\,\alpha_{T,s}\,\Delta T_j\,A_{s,j}\right], \\ &= \frac{1}{E_c\,A_{tr}} E_c\left[\int_{A_c} \alpha_{T,c}\,\Delta T\;\mathrm{d}A + n_E\sum_{j=1}^{L} \alpha_{T,s}\,\Delta T_j\,A_{s,j}\right], \\ &= \frac{1}{A_{tr}}\left[\int_{A_c} \alpha_{T,c}\,\Delta T\;\mathrm{d}A + n_E\sum_{j=1}^{L} \alpha_{T,s}\,\Delta T_j\,A_{s,j}\right], \end{aligned} \tag{3.27}$$

where $\alpha_{T,c}$ is the thermal expansion of concrete and $\alpha_{T,s}$ is the thermal expansion of steel.

The fifth step refers to bending moment M. It is energetically conjugate to the cross-sectional rotation $\partial w_0/\partial x$ and reads as

$$M = \int_A \sigma_{xx}\,z\;\mathrm{d}A\,, \tag{3.28}$$

Inserting Eq. (3.21) into (3.28) yields under consideration of (3.15):

$$\begin{aligned} M &= \int_A E\left(\varepsilon_0 + \kappa_0\,z - \alpha_T\Delta T\right) z\;\mathrm{d}A\,, \\ &= \underbrace{\int_A E\,z^2\;\mathrm{d}A}_{\overline{EI}}\;\kappa_0 - \underbrace{\int_A E\,\alpha_T\Delta T\,z\;\mathrm{d}A}_{\overline{EI}\,\kappa_0^e}\,, \\ &= \overline{EI}(\kappa_0 - \kappa_0^e)\,. \end{aligned} \tag{3.29}$$

Eq. (3.29) is the motivation to introduce the effective bending stiffness of the beam as

$$\overline{EI} = \int_A E\,z^2\;\mathrm{d}A\,. \tag{3.30}$$

In the case of a reinforced concrete beam, $\overline{EI}$ can be rewritten as

$$\begin{aligned}\int_A E\,z^2\;\mathrm{d}A &= \int_{A_c} E_c\,z^2\;\mathrm{d}A + \int_{A_s} E_s\,z^2\;\mathrm{d}A\,, \\ &= E_c I_c + E_c\,\underbrace{\frac{E_s}{E_c}}_{n_E}\sum_{j=1}^{L} A_{s,j}\,z_j^2\,, \\ &= E_c\underbrace{\left[I_c + n_E\sum_{j=1}^{L} A_{s,j}\,z_{s,j}^2\right]}_{I_{tr}}, \end{aligned} \tag{3.31}$$

where $I_{tr} = I_c + n_E\cdot\sum_{j=1}^{L} A_{s,j}\,z_{s,j}^2$ refers to the second moment of inertia of the "transformed" cross section, and $z_{s,j}$ refers to the distance between each individual reinforcement bar and the

axis of the beam. The eigencurvature of the axis of the beam is calculated according to Eq. (3.29) as

$$\kappa_0^e = \frac{1}{\overline{EI}} \int_A E\,\alpha_T \Delta T\, z \;\mathrm{d}A\,, \tag{3.32}$$

which in the case of a reinforced concrete beam that presents a constant temperature within each reinforcement bar, considering Eqs. (3.31) and (3.32), leads to

$$\begin{aligned}
\kappa_0^e &= \frac{1}{\overline{EI}} \left[\int_{A_c} E_c\,\alpha_{T,c}\,\Delta T\, z \;\mathrm{d}A + \sum_{j=1}^{L} E_s\,\alpha_{T,s}\,\Delta T_j\,A_{s,j}\,z_{s,j} \right] , \\
&\frac{1}{E_c\,I_{tr}} E_c \left[\int_{A_c} \alpha_{T,c}\,\Delta T\, z \;\mathrm{d}A + n_E \sum_{j=1}^{L} \alpha_{T,s}\,\Delta T_j\,A_{s,j}\,z_{s,j} \right] , \\
&= \frac{1}{I_{tr}} \left[\int_{A_c} \alpha_{T,c}\,\Delta T\, z \;\mathrm{d}A + n_E \sum_{j=1}^{L} \alpha_{T,s}\,\Delta T_j\,A_{s,j}\,z_{s,j} \right] .
\end{aligned} \tag{3.33}$$

The completed derivation underlines that the spatially nonlinear eigenstrain distribution $\alpha_T \Delta T$ can be decomposed into three contributions:

$$\alpha_T \Delta T = \varepsilon_0^e + \kappa_0^e\, z + \varepsilon_w^e\,. \tag{3.34}$$

In Eq. (3.34), ε_0^e denotes a spatially constant contribution according to Eq. (3.26), representing an eigenstretch of the beam; $\kappa_0^e\, z$ denotes a spatially linear contribution with vanishing mean value, see Eq. (3.32), representing an eigencurvature of the beam; and ε_w^e denotes the spatially non-linear rest of the eigenstrain distribution, representing an eigenwarping of the cross-section of the beam.

Thermal stresses are derived as follows: Eqs. (3.23) and (3.29), are rearranged as

$$\varepsilon_0 = \frac{N}{\overline{EA}} + \varepsilon_0^e\,, \tag{3.35}$$

$$\kappa_0 = \frac{M}{\overline{EI}} + \kappa_0^e\,. \tag{3.36}$$

Inserting Eqs. (3.35) and (3.36) into Eq. (3.21) yields

$$\begin{aligned}
\sigma_{xx}(y,z) &= E(y,z) \left[\left(\frac{N}{\overline{EA}} + \varepsilon_0^e \right) + \left(\frac{M}{\overline{EI}} + \kappa_0^e \right) z - \alpha_T(y,z)\Delta T(z) \right] \\
&= \frac{N\,E(y,z)}{\overline{EA}} + \frac{M\,E(y,z)}{\overline{EI}}\, z \underbrace{- E(y,z) \left[\alpha_T(y,z)\Delta T(z) - \varepsilon_0^e - \kappa_0^e\, z \right]}_{\sigma_w^e(y,z)} .
\end{aligned} \tag{3.37}$$

Thus, thermal stresses resulting from prevented eigenwarping of the cross-sections of the beam read as

$$\sigma_w^e(y,z) = -E(y,z) \left[\alpha_T(y,z)\Delta T(z) - \varepsilon_0^e - \kappa_0^e z \right] . \tag{3.38}$$

The expression in the square brackets of Eq. (3.38) is equal to the nonlinear part of the eigenstrains, ε_w^e, see Eq. (3.34).

3.2.2 Application to prismatic, reinforced concrete beams

Regarding the solution of the one-dimensional heat equation for one temperature increment prescribed at the top surface ΔT^{top} and constant temperature at the bottom surface of the structure in [2], the derivation of thermal stresses in prismatic beams with homogeneous material behavior is documented in [17]. In this case the solution is extended to the material behavior of reinforced concrete. The mechanical loads are acting in the x-z-plane, resulting in an axial force N and a bending moment $M_y = M$. The total stress to which the concrete is subjected results from inserting Eqs. (3.25) and (3.31) into Eq. (3.37), yielding

$$\sigma_{xx,c}(z) = \frac{N}{A_{tr}} + \frac{M}{I_{tr}}\, z \underbrace{-E_c\Big[\alpha_{T,c}\,\Delta T(z) - \varepsilon_0^e - \kappa_0^e\, z\Big]}_{\sigma_w^e(z)} . \tag{3.39}$$

Herein, the first term depending on axial force N refers to the influence of the eigenstretches, ε_0, on the total stress, the second term depending on bending moment M refers to the influence of the eigencurvature, κ_0, on the total stress, and the third term refers to the influence of the prevented eigenwarping on the total stress, see Eq. (3.38). Inserting the solution of the heat conduction problem of prismatic beams, described in Eq. (3.8) into Eq. (3.27) and (3.33) leads to the eigenstrain

$$\begin{aligned}\varepsilon_0^e =& \frac{1}{A_{tr}}\Bigg[A_c \sum_{k=1}^{N_T} \alpha_{T,c}\Delta T_k^{bot} \cdot \left(\frac{1}{2} - \sum_{n=1}^{\infty} \exp\left(-\frac{(2n-1)^2\pi^2 a\langle t - t_k\rangle}{h^2}\right)\frac{4}{(2n-1)^2\pi^2}\right) \\ &+ n_E\,\alpha_{T,s}\sum_{j=1}^{L}\Delta T_j A_{s,j}\Bigg],\end{aligned} \tag{3.40}$$

and the eigencurvature of a prismatic reinforced concrete beam

$$\begin{aligned}\kappa_0^e =& \frac{1}{I_{tr}}\Bigg[-I_c \sum_{k=1}^{N_T} \alpha_{T,c}\Delta T_k^{bot}\left(\frac{1}{h} - \sum_{n=1}^{\infty} \exp\left(-\frac{(2n\pi)^2 a\langle t - t_k\rangle}{h^2}\right)\frac{6}{(n\pi)^2}\frac{1}{h}\right) \\ &+ n_E\,\alpha_{T,s}\sum_{j=1}^{L}\Delta T_j A_{s,j}\, z_j\Bigg].\end{aligned} \tag{3.41}$$

Thus, the self-equilibrated stresses resulting from prevented eigenwarping of the cross-section of a prismatic, reinforced concrete beam as defined in the expression in the square brackets of Eq. (3.39) considering Eqs. (3.40) and (3.41) reads, as

$$\begin{aligned}\sigma_w^e(z) = E_c\Bigg[&\sum_{k=1}^{N_T}\alpha_{T,c}\,\Delta T_k^{bot}\Bigg\{\frac{1}{2}\left(1 - \frac{A_c}{A_{tr}}\right) + \frac{z}{h}\left(1 - \frac{I_c}{I_{tr}}\right) + \sum_{n=1}^{\infty}\Bigg\{ \\ &+ \exp\left(-\frac{(2n-1)^2\pi^2 a\langle t - t_k\rangle}{h^2}\right)\left[\frac{2(-1)^n}{(2n-1)\pi}\cos\left(-(2n-1)\pi\frac{z}{h}\right) + \frac{A_c}{A_{tr}}\frac{4}{(2n-1)^2\pi^2}\right] \\ &- \exp\left(-\frac{(2n\pi)^2 a\langle t - t_k\rangle}{h^2}\right)\left[\frac{(-1)^n}{n\pi}\sin\left(-2n\pi\frac{z}{h}\right) - \frac{I_c}{I_{tr}}\frac{6}{(n\pi)^2}\frac{z}{h}\right]\Bigg\}\Bigg\} \\ &- n_E\,\alpha_{T,s}\sum_{j=1}^{L}\Delta T_j\left(\frac{A_{s,j}}{A_{tr}} - \frac{A_{s,j}}{I_{tr}}\, z_{s,j}\, z\right)\Bigg].\end{aligned} \tag{3.42}$$

3.2.3 Application to cylindrical, reinforced concrete columns

In consideration of the boundary conditions between columns and slabs, both internal forces, the axial force N and the bending moment M exist. A cylindrical coordinate system with origin at the axis of the column is suitable for the description of the axisymmetric cross-section. The transformation of the Cartesian coordinate z to cylindrical coordinates reads as

$$z = r\,\sin(\varphi)\,, \tag{3.43}$$

where r is the radial coordinate with origin at the beam axis and φ is the angular coordinate with respect to the y-axis of a local Cartesian coordinate system, see Fig. 3.2. The total stress to which the concrete is subjected results from inserting Eqs. (3.43), (3.25) and (3.31) into Eq. (3.37), yielding

$$\sigma_{xx,c}(r,\varphi) = \frac{N}{A_{tr}} + \frac{M}{I_{tr}}\,r\,\sin(\varphi) \underbrace{-E_c\Big[\alpha_{T,c}\Delta T(r) - \varepsilon_0^e\Big]}_{\sigma_w^e(r,\varphi)}\,, \tag{3.44}$$

where the linear part of the eigenstrains κ_0^e is equal to zero, because of the boundary conditions in temperature of the lateral surface. In this case, the stresses from prevented eigenwarping depend only on the thermal eigenstretches of the axis. Inserting Eq. (3.13) into Eq. (3.27) yields

$$\begin{aligned}\varepsilon_0^e = \alpha_{T,c}\frac{A_c}{A_{tr}}\Bigg[\Delta T^{lat} + \sum_{k=1}^{N_T}\frac{4(T_{ref} - \Delta T_k^{lat})}{R^2}\sum_{n=1}^{\infty}\frac{1}{\lambda_n^2}\exp(-\lambda_n^2 a\langle t - t_k\rangle)\Bigg] \\ + n_E\,\alpha_{T,s}\sum_{j=1}^{L}\frac{A_{s,j}}{A_{tr}}\Delta T_j\,.\end{aligned} \tag{3.45}$$

Thus, the self-equilibrated stresses resulting from prevented eigenwarping of the cross-section of a cylindrical reinforced concrete column as defined in the expression in the square brackets of Eq (3.44) considering Eq. (3.45) reads, as

$$\begin{aligned}\sigma_w^e(r) = E_c\Bigg[&\alpha_{T,c}\,\Delta T^{lat}\left(1 - \frac{A_c}{A_{tr}}\right) \\ &+ \sum_{k=1}^{N_T}\frac{4(T_{ref} - \Delta T_k^{lat})}{R^2}\sum_{n=1}^{\infty}\frac{1}{\lambda_n}\left(\frac{R}{2}\frac{J_0(\lambda_n r)}{J_1(\lambda_n R)} - \frac{A_c}{A_{tr}}\frac{1}{\lambda_n}\right)\exp(-\lambda_n^2 a\langle t - t_k\rangle) \\ &- n_E\,\alpha_{T,s}\sum_{j=1}^{L}\frac{A_{s,j}}{A_{tr}}\Delta T_j\Bigg]\,.\end{aligned} \tag{3.46}$$

Regarding the solution of radial heat conduction in Eq. (3.13), the derivation of thermal stresses in cylindrical columns is documented in Appendix B.

3.3 Engineering mechanics modeling at the structural scale

In thermoelasticity the internal forces M and N depend on the eigenstretch and eigencurvature ε_0^e and κ_0^e, see Eqs. (3.23) and (3.29):

$$N = \overline{EA}\,(\varepsilon_0 - \varepsilon_0^e)\,, \qquad M = \overline{EI}\,(\kappa_0 - \kappa_0^e)\,. \tag{3.47}$$

In statically determinate structures, the thermal eigenstretches ε_0^e and eigencurvatures κ_0^e are free to develop. Thus, there are no internal forces. As a consequence, the total internal forces depend on the mechanical loading only. In case of a statically *in*determinate structure, the boundary conditions constrain the thermal eigenstretches and eigencurvatures. Corresponding stresses need to be quantified based on a simulation of the behavior of the whole structure, accounting for its boundary conditions. The tested structure described in Chapter 2 and [7] will be modeled with the beam analysis software RStab [8] using first-order beam theory.

In a first step, the three-dimensional FE model produced in Abaqus CAE [6], see Fig. 2.2a and Fig. 2.4, will be used as a basis in order to build a simplified one-dimensional beam model. For this purpose, the structure will be idealized as located on the axis of each cross-section. Rigid connections between the structural elements are assumed. The resulting structure consists of a three-span frame formed by top slab, bottom slab, and walls with two columns that separate the cells. In order to perform the simulation as simple as possible and as complex as necessary, the tapered part of the top slab will not be part of the model. This yields an idealized structure for the simulation with beam analysis software which is statically indeterminate to the twelfth degree ($n = 12$), see Fig. 3.3. The local coordinate system of the frame is defined by the dashed line, see Fig 3.2. x_j, with $j = 1, 2, \ldots, 12$, denotes axial locations at which results will be discussed.

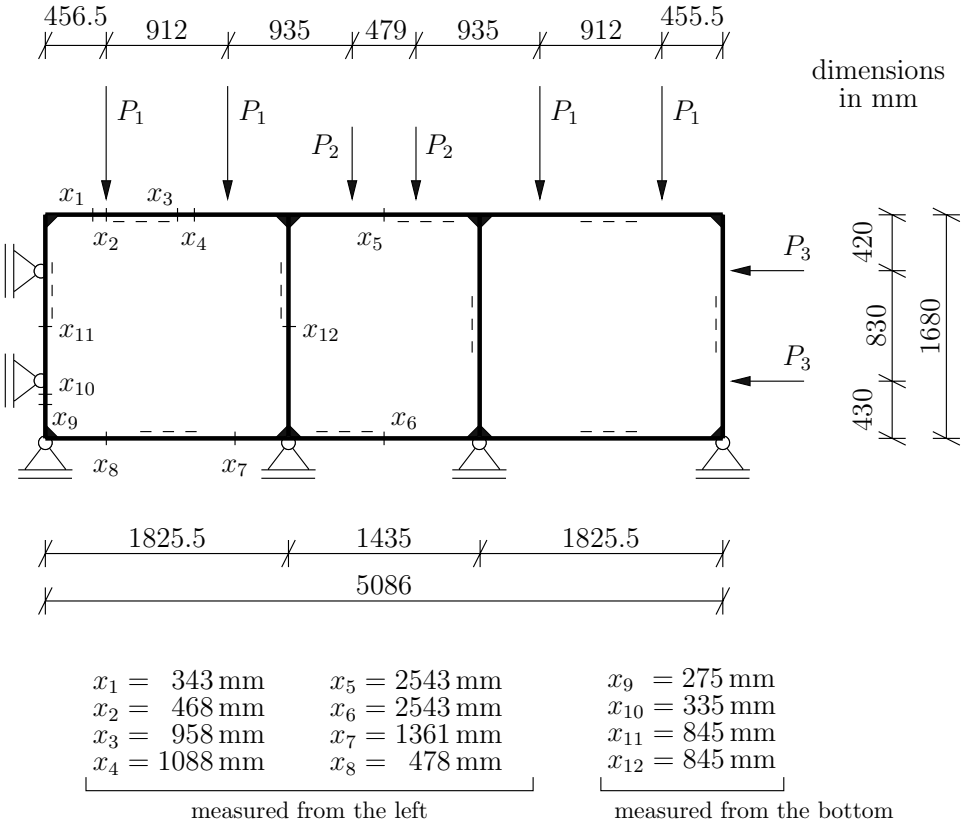

Fig. 3.3: Idealized representation of the tested segment of a subway station, as the basis for structural analysis using beam analysis software: for the numerical values of the point loads P_1, P_2, and P_3 see Table 2.1.

In a second step, the cross-section of the columns is transformed from its prismatic shape with dimension 160/240 mm to a circular shape with diameter $D = 221.116$ mm, equivalent in extensional stiffness. The expectation of a predominance of axial force at the columns provides the motivation for performing the transformation of the columns from a rectangular cross-section

to a circular one with equivalent extensional stiffness. The verification of this transformation will be discussed in comparison with the results.

In a third step, the reinforced concrete cross-sections of the structure will be idealized as transformed cross-sections depending on the material behavior of concrete as defined in Eqs (3.25) and (3.31). This reads as

$$\begin{aligned} A_{tr} &= A + (n_E - 1)\, A_s \,, \\ & \qquad\qquad \text{with} \quad n_E = \frac{E_s}{E_c} = 5.838 \,, \\ I_{tr} &= I + I_s\,(n_E - 1) + \sum_{j=1}^{L} A_{s,j}\, z_{s,j}^2\, n_E \,, \end{aligned} \tag{3.48}$$

where A denotes the real area defined as $A = A_c + A_s$ and I denotes the real second moment of inertia defined as $I = I_c + I_s$. The "transformed" cross-sectional properties are input for the beam analysis software RStab [8]. This requires the quantification of ratio factors defined as

$$\eta_A = \frac{A_{tr}}{A} \,, \qquad \eta_I = \frac{I_{tr}}{I} \,. \tag{3.49}$$

The ratio factors of each part of the structure as defined in Eq. (3.49) are documented in Table 3.1, see also [7] and Section 2.2. Material properties that are required for simulation with beam

Tab. 3.1: Cross-sectional properties of the structural elements: "transformed properties" refer to a cross-section consisting of concrete only, but being equivalent to the actual reinforced concrete cross-section, "real properties" refer to the actual concrete part of the actual cross-section, "ratio factors" are defined in Eq. (3.49)

cross-section	**transformed property** A_{tr} [mm^2], I_{tr} [mm^4]	**real property** A [mm^2], I [mm^4]	**ratio factors** [-], see Eq. (3.49)
Top Slab	$A_{tr} = 2.684 \times 10^5$ $I_{tr} = 1.037 \times 10^9$	$A = 2.520 \times 10^5$ $I = 9.261 \times 10^8$	$\eta_A = 1.065$ $\eta_I = 1.120$
Bottom Slab	$A_{tr} = 2.411 \times 10^5$ $I_{tr} = 7.529 \times 10^8$	$A = 2.280 \times 10^5$ $I = 6.859 \times 10^8$	$\eta_A = 1.058$ $\eta_I = 1.098$
Lateral Wall	$A_{tr} = 2.279 \times 10^5$ $I_{tr} = 6.073 \times 10^8$	$A = 2.100 \times 10^5$ $I = 5.359 \times 10^8$	$\eta_A = 1.085$ $\eta_I = 1.133$
Columns	$A_{tr} = 4.387 \times 10^4$ $I_{tr} = 1.388 \times 10^8$	$A = 3.840 \times 10^4$ $I = 1.173 \times 10^8$	$\eta_A = 1.143$ $\eta_I = 1.183$

analysis software RStab [8] based on the simulation with FE software ABAQUS CAE in [7] are documented in Tables 2.2 and 2.3.

Chapter 4

Results and discussion

The structural behavior of a segment of a subway station, subjected to (i) mechanical loading simulating ground pressure and (ii) thermal loading representative for a moderate fire, see Chapter 2 and [7, 21] for details, is analyzed with methods from engineering thermoelasticity. The analysis starts with simulating transient heat conduction from the heated inner surfaces into the volume of the structural elements.

4.1 Results from the simulation of heat conduction

The transient heat conduction problem described in Section 3.1 is solved by inserting the thermal properties of concrete from Table 2.2 and the surface temperature histories illustrated in Fig. 2.5 into the derived semi-analytical solutions, see Eqs. (3.8) and (3.13). The infinite sums are approximated based on the first 1000 terms. This is more than sufficient to obtain a well-converged solution. The obtained results are illustrated as solid lines in Fig. 4.1. They are compared with results from the FE simulation by Diaz et al. [7], see the dashed lines in Fig. 4.1.

For the slabs and the walls, similar results are obtained, see Figs. 4.1a–c. During half an hour of heating, the heat front penetrates into the inner half of the structural elements, while the temperature in the outer half remains in good approximation equal to the initial value. The increase of the temperature suggested by the FE model is slightly larger than that obtained with the engineering mechanics model. The temperature distribution obtained with the engineering mechanics model is smooth, while the one from the FE simulation is piecewise linear.

As for the columns, a direct comparison of results obtained from the FE analysis (prismatic cross-section) with results obtained from the engineering mechanics model (idealized circular cross-section) is made feasible based on normalized coordinates:

$$z_n = \frac{z}{h}\,, \qquad z_n = \frac{y}{b}\,, \qquad z_n = \frac{r}{R}\,, \tag{4.1}$$

where z_n denotes the normalized coordinate, y and z stand for the Cartesian coordinates of the prismatic cross-section of the actual columns with width $b = 240\,\text{mm}$ and height $h = 160\,\text{mm}$, and r is the radial coordinate of the cylindrical cross-section of the idealized column with radius $R = 110.6\,\text{mm}$, see also Fig. 4.1d. The FE simulation and the engineering mechanics analysis deliver similar results which are qualitatively similar, but quantitatively different. The increase of temperature at the axis of the columns, predicted by the FE model, amounts to 44°C. The corresponding results of the engineering mechanics model is equal to 14.5°C. This is a consequence of the cross-sectional transformation. The ingress of heat into the cylindrical column is axisymmetric; the distance from the surface to the center is uniform and amounts to 110.6 mm. As for the actual column with prismatic cross-section, in turn, heat transport is biaxial problem, and the distance from the closer lateral surface to the center amount to 80 mm. Therefore, the center of the prismatic cross-section heats up faster than that of the circular one.

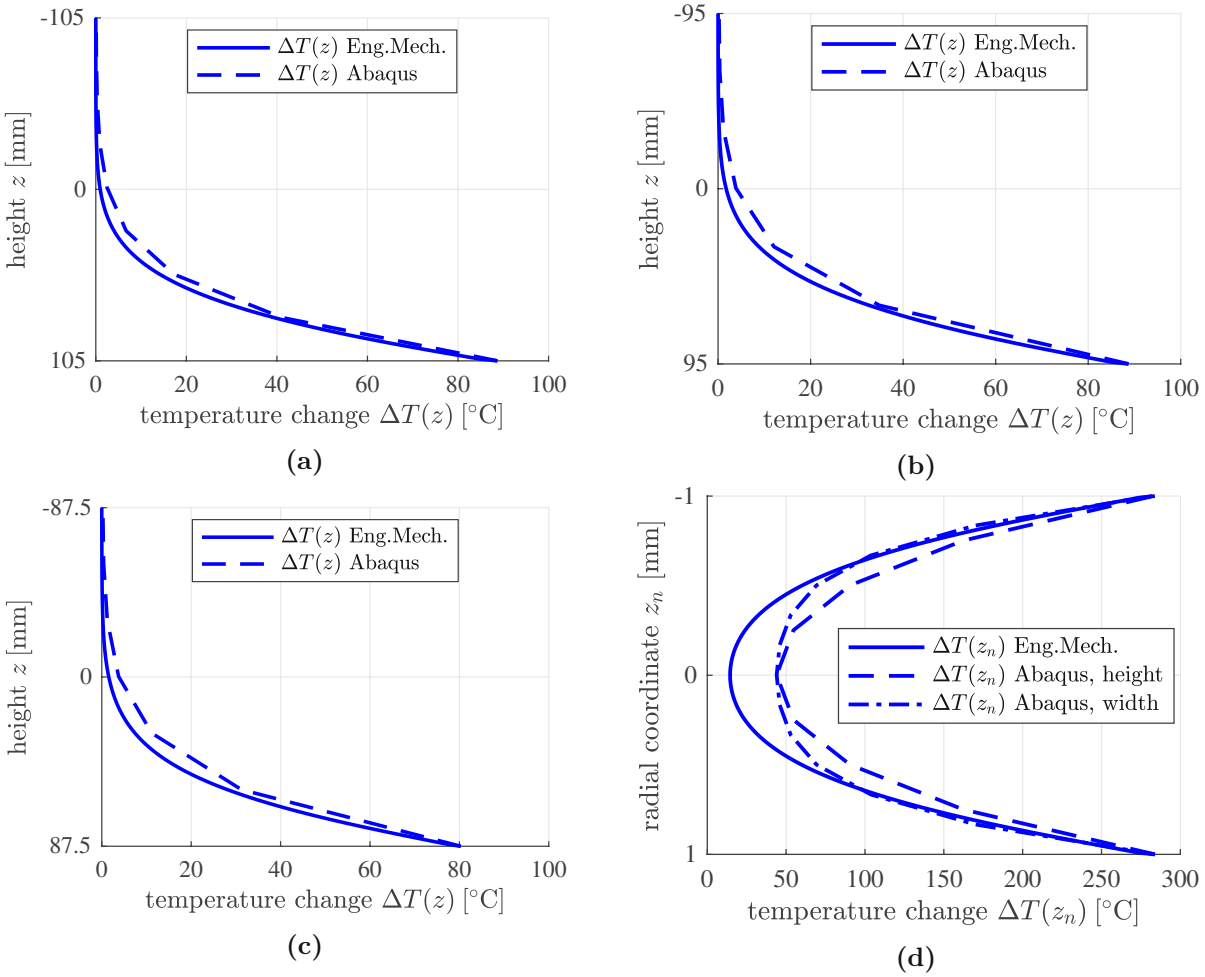

Fig. 4.1: Temperature changes half an hour after the start of the fire of **(a)** the top slab, **(b)** the bottom slab, **(c)** the left wall, and **(d)** the left column, obtained with the engineering mechanics analysis, see the solid lines, and with the FE model, see the dashed and dash-dotted lines.

4.2 Decomposition of thermal eigenstrains

In order to compute thermal eigenstrains for all structural elements, the temperature changes illustrated in Figs. 4.1 are multiplied with the coefficients of thermal expansion of steel and concrete; see the dotted red lines in Figs. 4.2 for the eigenstrain distributions experienced by concrete. These spatially nonlinear distributions are subdivided into (i) a constant part, related to the eigenstretch, ε_0^e, of the axis of the structural element, see Eq. (3.26) and (3.27) as well as the blue solid lines in Figs. 4.2, (ii) a linear part, related to the eigencurvature, κ_0^e, of the axis of the structural element, see Eqs. (3.32) and (3.33) as well as the blue dashed lines in Figs. 4.2, and (iii) the nonlinear rest, representing the thermal eigenwarping of the cross-section of the structural element:

$$\varepsilon_w^e = \alpha_T \Delta T - \varepsilon_0^e - \kappa_0^e \, z \,, \tag{4.2}$$

and the dash-dotted blue lines in Figs. 4.2. The numerical values of the eigenstretches and eigencurvatures are listed in Table 4.1.

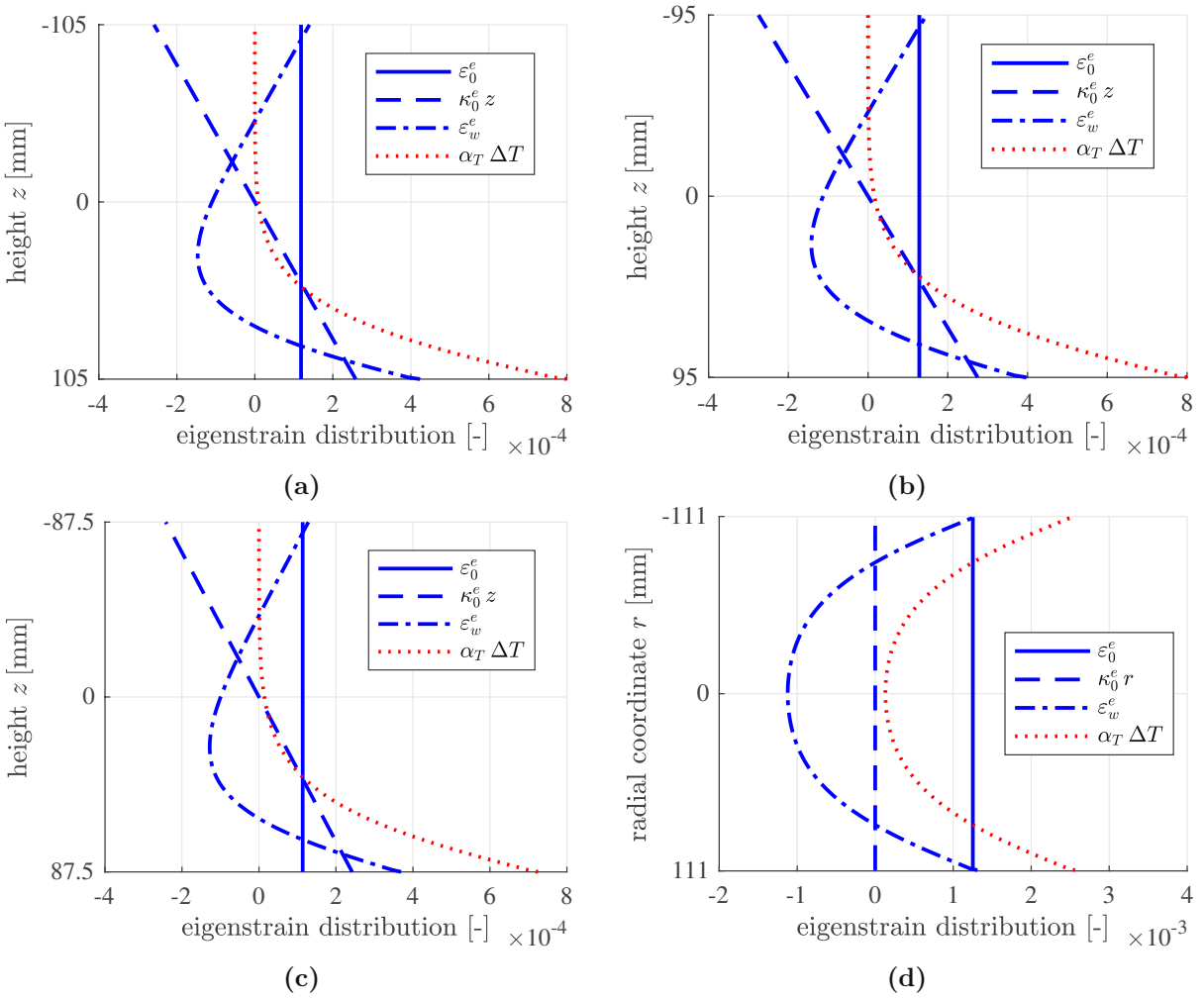

Fig. 4.2: Thermal eigenstrains of concrete half an hour after the start of the fire of **(a)** the top slab, **(b)** the bottom slab, **(c)** the left wall, and **(d)** the left column, obtained with the engineering mechanics analysis: the dotted graphs refer to total eigenstrains, the solid graphs to the eigenstretch, the dashed graphs to the eigencurvature, and the dash-dotted graphs to the eigenwarping of the cross-section of the structural element.

Tab. 4.1: Numerical values of the thermal eigenstretches and eigencurvatures of the axes of the structural elements, half an hour after the start of the fire, obtained with the engineering mechanics approach, see Eqs. (3.27) and (3.33).

Cross-section	**Eigenstretch** $[10^{-4}]$	**Eigencurvature** $[10^{-6}\,\mathrm{mm}^{-1}]$
Top Slab	$\varepsilon_0^e = \ \ 1.1848$	$\kappa_0^e = 2.4632$
Bottom Slab	$\varepsilon_0^e = \ \ 1.2860$	$\kappa_0^e = 2.8946$
Lateral Wall	$\varepsilon_0^e = \ \ 1.1362$	$\kappa_0^e = 2.7662$
Columns	$\varepsilon_0^e = 12.5200$	$\kappa_0^e = 0.0000$

4.3 Structural analysis using beam analysis software

Two simulations are carried out. The first one refers to the point loads representing ground pressure. This simulation provides insight into the structural behavior before the start of the fire. The second simulation refers to the point loads representing ground pressure *and* eigenstretches as well as eigencurvatures representing the thermal loading half an hour after the start of the fire. The differences of the results of the two simulations, regarding the axial forces and bending moments, refer to load redistributions resulting from the fire.

4.3.1 Mechanical loading simulating service conditions

The structural model is subjected to point loads P_1, P_2, and P_3, see Table 2.1. The internal forces obtained with beam analysis software RStab [8] are nearly symmetrical with respect to a column-parallel axis through the center of the structure, see Figs. 4.3 and 4.4.

The largest absolute values of the bending moments range from 52 kNm to 65 kNm. They are activated in the top slap, at the connections with the walls and the columns, see Fig. 4.3. The bending moments of the bottom slab are significantly smaller. Despite the rigid connections between the columns and the slabs, the bending moments in the columns are almost equal to zero.

The axial forces are negative and constant throughout every structural element, see Fig. 4.4. The axial force of the top slab is larger than that of the bottom slab. The largest compressive axial forces are activated in the columns. This confirms, a posteriori, the assumption that the axial force would be dominant in the columns. Notably, this assumption provided the motivation for transforming the rectangular columns into circular ones, such that the extensional stiffness is the same.

4.3.2 Mechanical and thermal loading representative for a moderate tunnel fire

The structural model is subjected to point loads P_1, P_2, and P_3, see Table 2.1, and to eigenstretches and eigencurvatures representative for the time instant half an hour after the start of the fire, see Table 4.1. The internal forces obtained with beam analysis software RStab [8] are nearly symmetrical with respect to a column-parallel axis through the center of the structure, see Figs. 4.5 and 4.6.

Because of the fire, the bending moments are significantly increased throughout the structure. The largest absolute values of the bending moments range from 91 kNm to 166 kNm. They are activated in the top slap, at the connections with the walls and the columns, see Fig. 4.5. The bending moments of the bottom slab are also significant, ranging from −61.4 kNm to −78.3 kNm. Despite the rigid connections between the columns and the slabs, the bending moments in the columns remain small.

The redistributions of the axial forces is governed by the eigenstretches of the columns, which are by one order of magnitude larger than the eigenstretches of the walls. Because the expansion of the columns is constrained, their compressive axial forces rise, during the first half an hour of the fire, from some −335 kN to some −385 kN. This goes along with a reduction of the axial forces of the walls from −200 kN to some −150 kNm. In addition, the compressive axial forces of the top slab are decreased by some 20 kN and redistributed to the bottom slab.

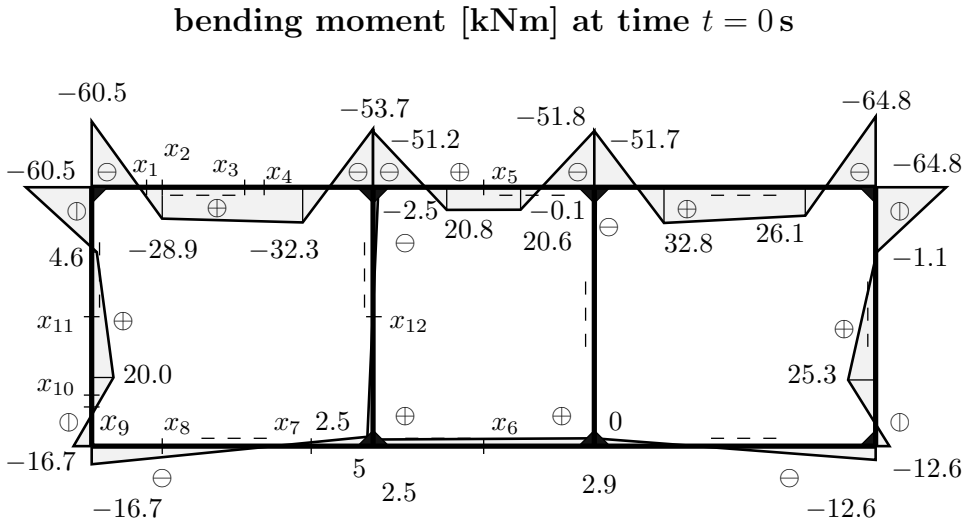

Fig. 4.3: Bending moments activated by the point loads listed in Table 2.1: simulation results obtained with RStab.

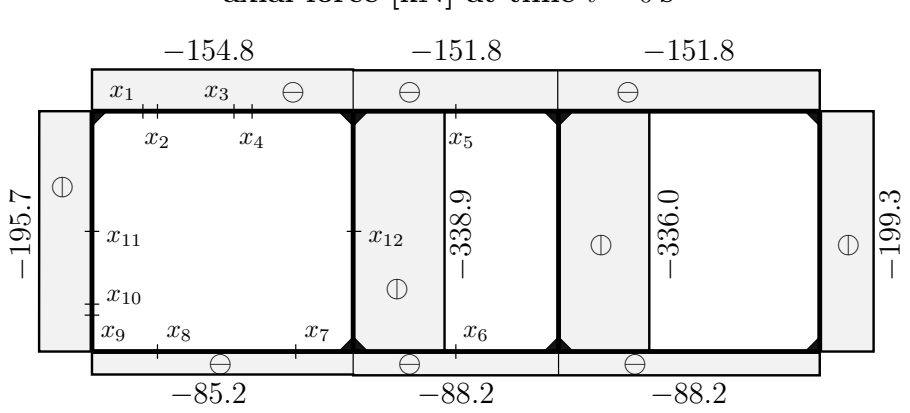

Fig. 4.4: Axial forces activated by the point loads listed in Table 2.1: simulation results obtained with RStab.

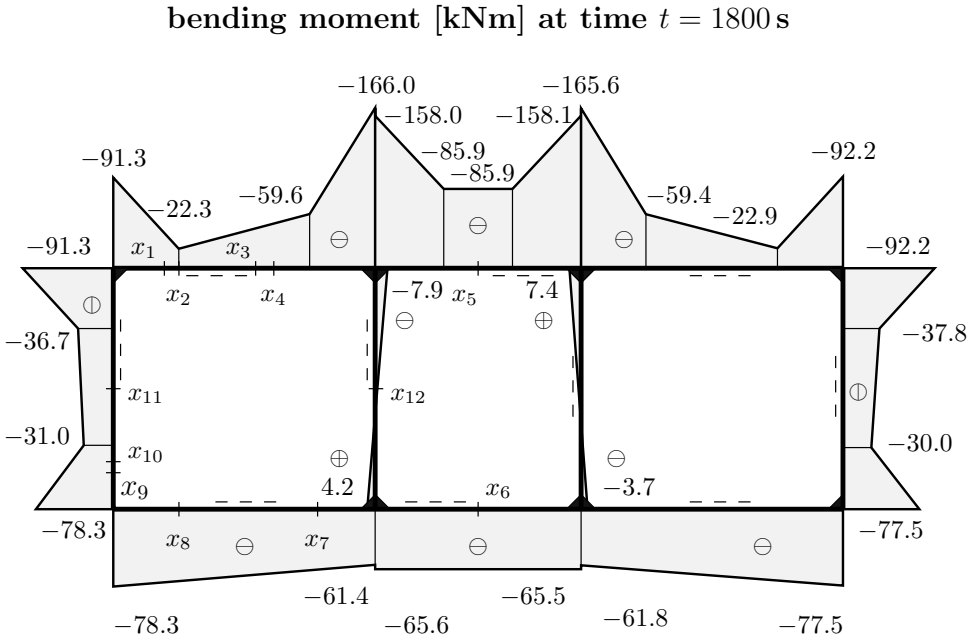

Fig. 4.5: Bending moments activated by the point loads listed in Table 2.1 and by fire-induced eigenstretches and eigencurvatures listed in Table 4.1: simulation results obtained with RStab.

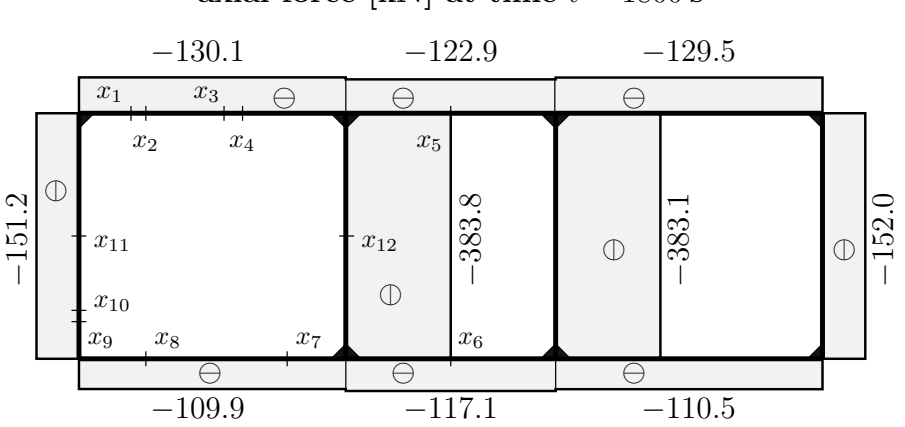

Fig. 4.6: Axial forces activated by the point loads listed in Table 2.1 and by fire-induced eigenstretches and eigencurvatures listed in Table 4.1: simulation results obtained with RStab.

4.4 Stress distributions at selected cross-sections

Under combined mechanical and transient thermal loading, axial stresses result, in every cross-section, from three contributions: the axial force, the bending moment, and eigenstresses. In the present context of reinforced concrete members, we focus on the axial stresses experienced by the concrete. The axial force refers to spatially constant axial stresses, the bending moment to spatially linear stresses, and the eigenstresses are nonlinearly distributed across the cross-section. The axial forces and the bending moments depend on the mechanical loading as well as the thermal eigenstretches and the eigencurvatures of all structural members. These contributions are accounted for by means of the simulation with the beam analysis software, see Section 4.3. The eigenstresses account for the *transient* nature of the heat conduction problem. They are equal to the eigenwarping-part of the thermal eigenstrains, multiplied with the modulus of elasticity and -1. The eigenwarping-parts of the thermal eigenstrains were determined in Section 4.2.

Axial stresses at selected cross-sections will be illustrated, in the following subsections, by means of two diagrams. The left diagram displays, with blue graphs, the stress distribution $\sigma_{xx,c}$ of concrete resulting from the point loads only, referring to the service condition *before* the fire. The right diagram displays, with red graphs, the stresses of concrete computed for the time instant half an hour after the start of the fire. In both cases, results from the simulation with beam analysis software, from the engineering mechanics analysis, and from FE simulation are compared.

4.4.1 Top slab

As for the top slab, cross-sectional stresses are discussed at the positions x_1 to x_5, see Fig. 3.3. In general, the stresses obtained with the FE simulation are well reproduced based on the engineering mechanics model, both qualitatively and quantitatively, see Figs. 4.7–4.11.

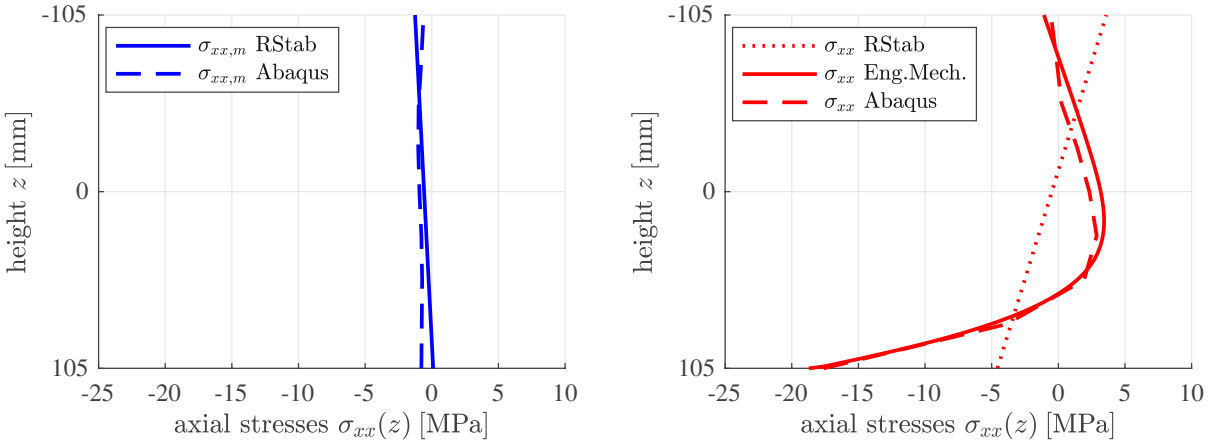

Fig. 4.7: Top slab location $x_1 = 0.343\,\text{m}$: axial stresses of concrete **(a)** before the fire, and **(b)** half an hour after the start of the fire.

As for the situation before the fire, the stress distributions obtained from the FE simulation and from the engineering mechanics analysis are virtually linear and perfectly linear, respectively. The kink of the stress distributions obtained with the FE model close to the upper surface at position x_2, see Fig. 4.8a, can be explained by the point load P_1 imposed at that position. This underlines that the Bernoulli-Euler hypothesis is questionable in the immediate vicinity of

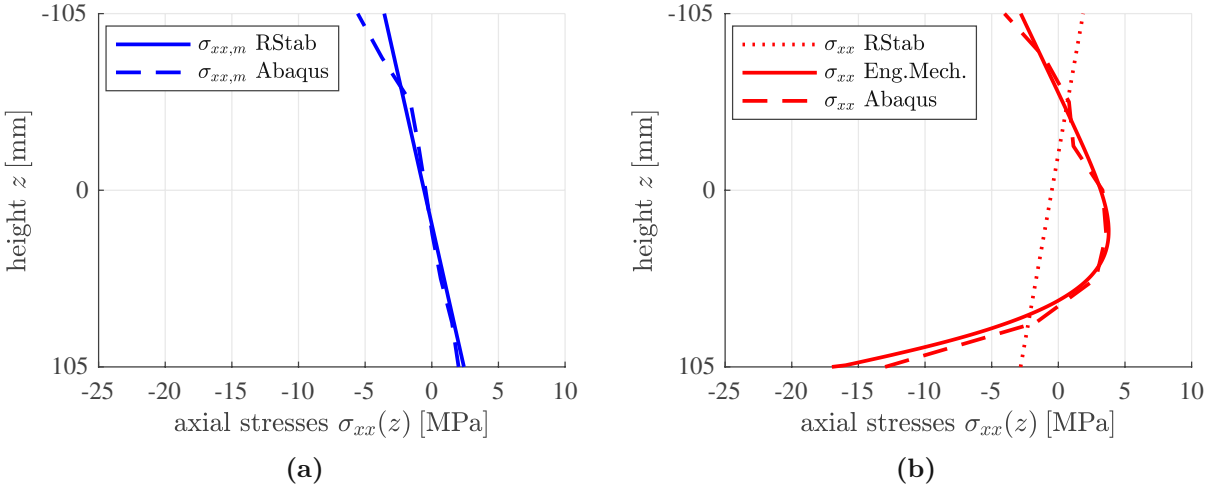

Fig. 4.8: Top slab location $x_2 = 0.468\,\text{m}$: axial stresses of concrete **(a)** before the fire, and **(b)** half an hour after the start of the fire.

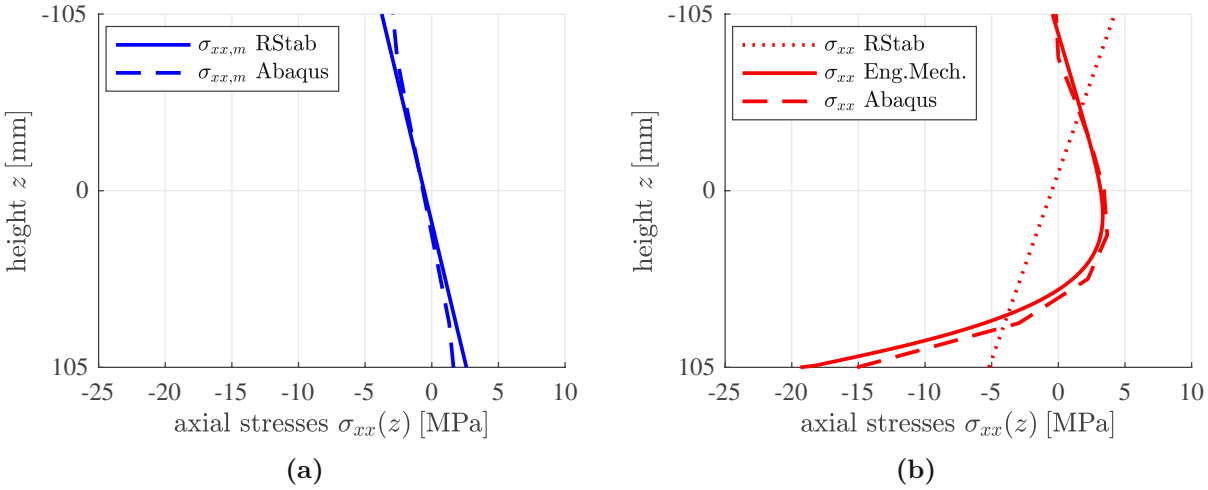

Fig. 4.9: Top slab location $x_3 = 0.958\,\text{m}$: axial stresses of concrete **(a)** before the fire, and **(b)** half an hour after the start of the fire.

concentrated loads. Still, the engineering mechanics analysis is reproducing the overall structural behavior very well.

As for the time instant half an hour after the start of the fire, the total stresses are nonlinearly distributed over the height of the cross-section. It is appealing that the engineering mechanics analysis allows for a decomposition of the total stresses into (i) spatially linear stress contributions resulting from the axial forces and the bending moments, as well as (ii) spatially nonlinear stress contributions resulting from the prevented eigenwarping of the cross-sections, see the similarity between the dash-dotted graphs in Fig. 4.2 and the dashed red graphs in Figs. 4.7b–4.11b. Both simulation approaches suggest that the maximum tensile stresses are activated inside the volume of the top slab rather than at the upper or lower surface. These tensile stresses amount to some 3 MPa. It is to be expected that the tensile strength of concrete would be reached shortly during the third quarter of an hour after the start of the fire, and that cracking of concrete will occur

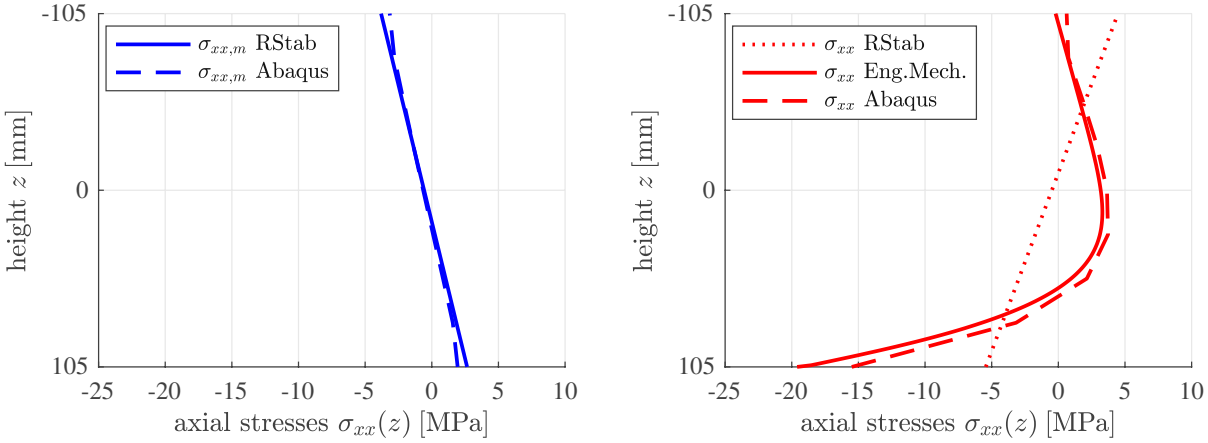

Fig. 4.10: Top slab location $x_4 = 1.088\,\text{m}$: axial stresses of concrete **(a)** before the fire, and **(b)** half an hour after the start of the fire.

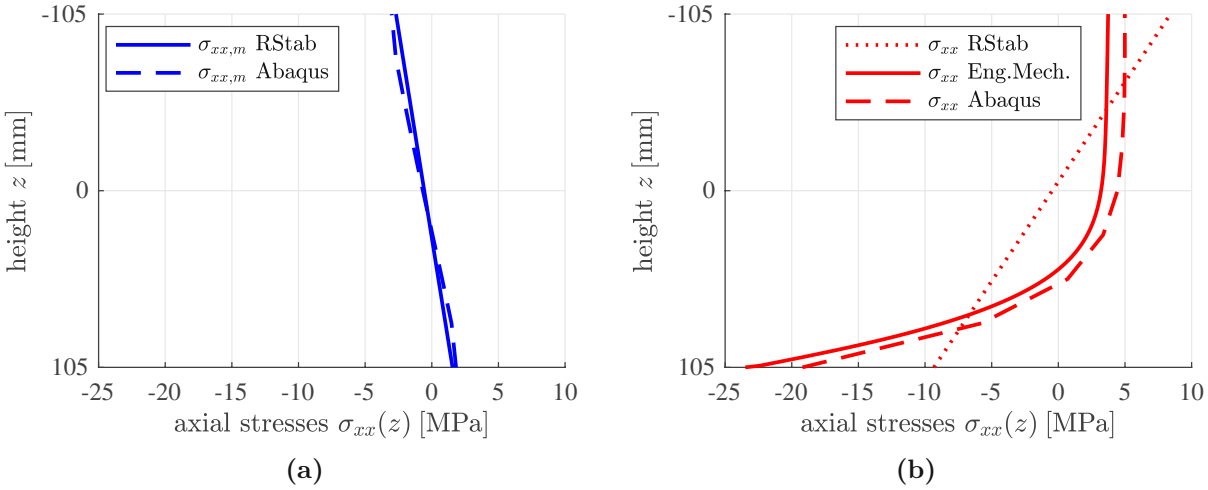

Fig. 4.11: Top slab location $x_4 = 2.543\,\text{m}$: axial stresses of concrete **(a)** before the fire, and **(b)** half an hour after the start of the fire.

visually unnoticeable *inside* the bulk of the top slab. At position x_5, the total stresses of the engineering model are qualitatively similar but quantitatively more compressive and less tensile compared to those of the FE model, see Fig. 4.11b. This implies that the differences originates from the constant part of the stresses, i.e. from the compressive axial force of the top slab, which is larger in the engineering mechanics model than in the FE model.

4.4.2 Bottom slab

As for the bottom slab, cross-sectional stresses are discussed at the positions x_6 to x_8, see Fig. 3.3. In general, the stresses obtained with the FE simulation are well reproduced based on the engineering mechanics model, both qualitatively and quantitatively, see Figs. 4.12–4.14.

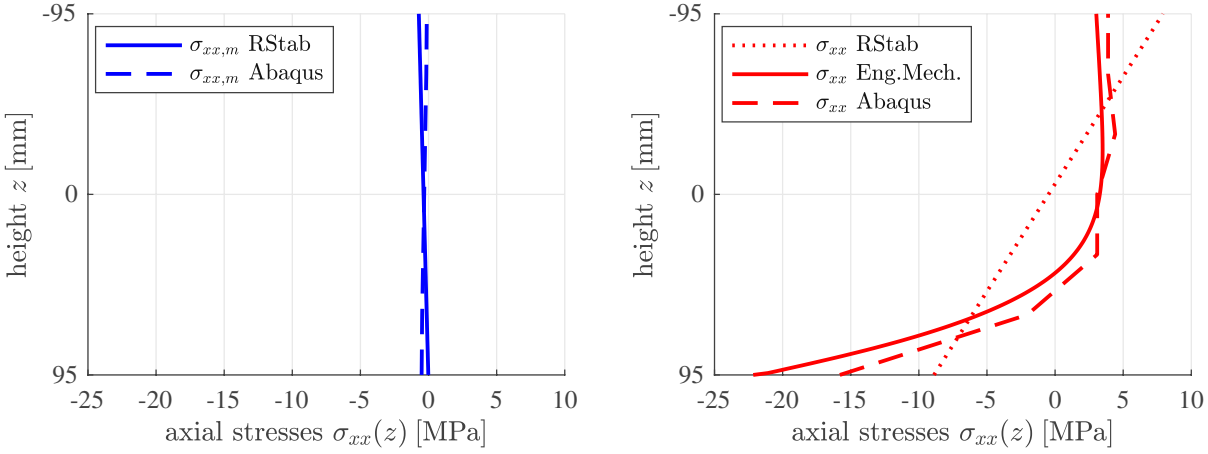

Fig. 4.12: Bottom slab location $x_6 = 2.543\,\text{m}$: axial stresses of concrete **(a)** before the fire, and **(b)** half an hour after the start of the fire.

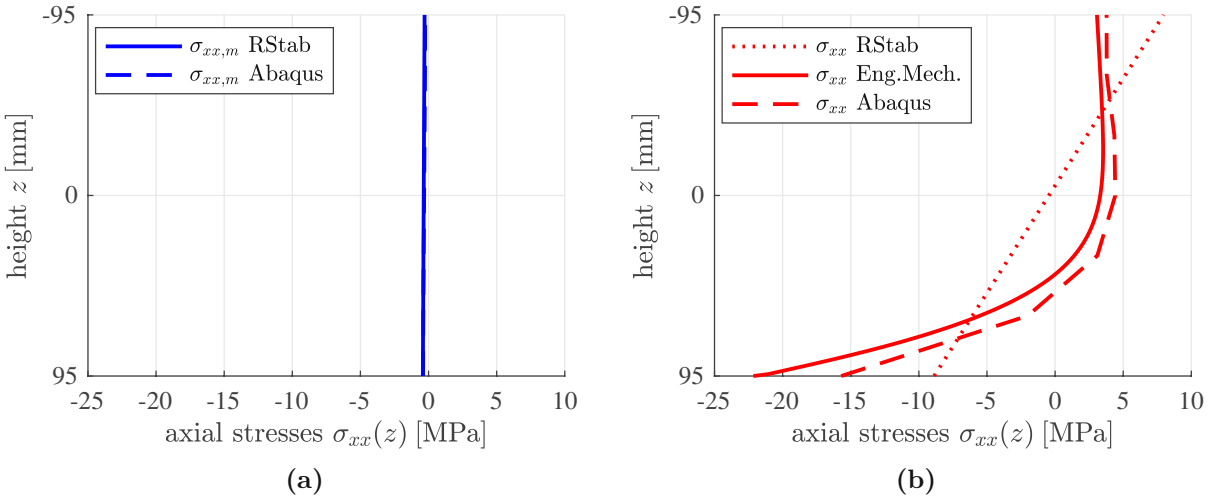

Fig. 4.13: Bottom slab location $x_7 = 1.361\,\text{m}$: axial stresses of concrete **(a)** before the fire, and **(b)** half an hour after the start of the fire.

As for the situation before the fire, the bottom slab experiences smaller axial forces and smaller bending moments than the top slab, see Figs. 4.3 and 4.4. This manifests itself in smaller stresses at positions x_6 to x_8 compared to the stresses at positions x_1 to x_5, see Figs. 4.7a–4.14a.

As for the time instant half an hour after the start of the fire, the effect described at position x_5 of the top slab is also found at positions x_6 and x_7 of the bottom slab: the stress distributions of the engineering mechanics model and the FE model appear to be quite parallel, whereby more compressive and less tensile stresses are obtained with the engineering mechanics model, compare Fig. 4.11b with Figs. 4.12b and 4.13b. At position x_8 the engineering mechanics model suggest larger compressive stresses at the bottom surface, correct stresses at the axis of the structural element, and smaller tensile stresses at the top surface, compared to the FE model. Thus, the difference appears to be related to the linear part of the stress distribution, which is related to the bending moment. Most importantly, the maximum tensile stress obtained in both approaches

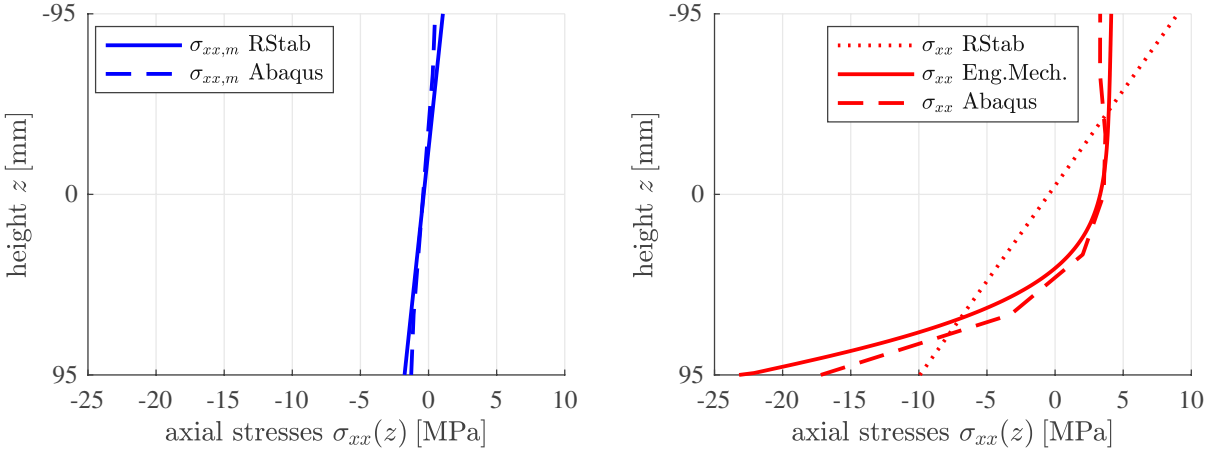

Fig. 4.14: Bottom slab location $x_8 = 0.478\,\text{m}$: axial stresses of concrete **(a)** before the fire, and **(b)** half an hour after the start of the fire.

are very similar at all three analyzed positions. This is particularly important for the question whether or not tensile cracking of concrete occurs.

4.4.3 Left wall

As for the left wall, cross-sectional stresses are discussed at the positions x_9 to x_{11}, see Fig. 3.3. In general, the stresses obtained with the FE simulation are well reproduced based on the engineering mechanics model, both qualitatively and quantitatively, see Figs. 4.15–4.17. Most importantly, the maximum tensile stress obtained in both approaches are very similar at all three analyzed positions, half an hour after the start of the fire, see Figs. 4.15b–4.17b. This is particularly important for the question whether or not tensile cracking of concrete occurs.

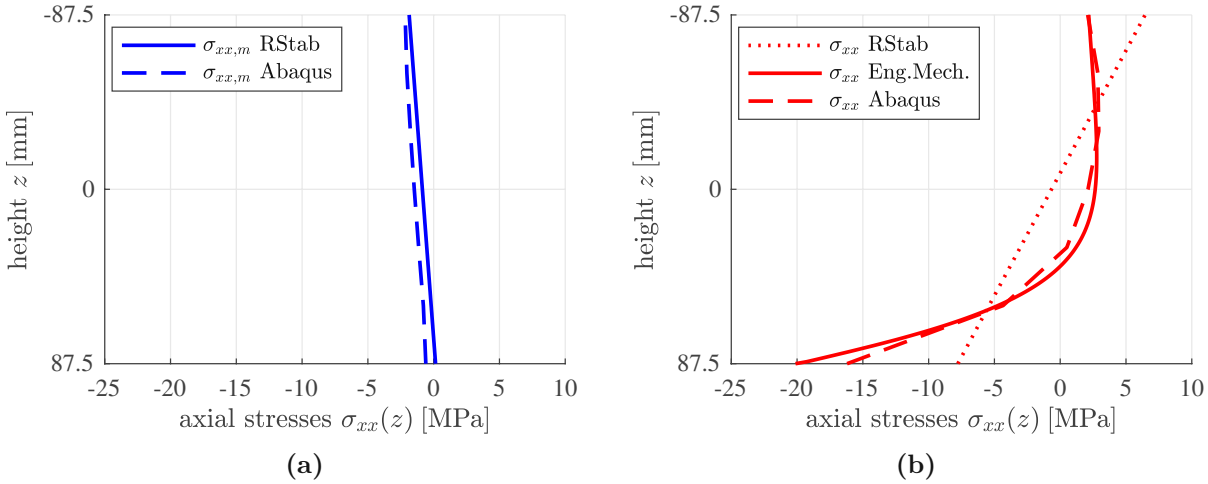

Fig. 4.15: Left wall location $x_9 = 0.275\,\text{m}$: axial stresses of concrete **(a)** before the fire, and **(b)** half an hour after the start of the fire.

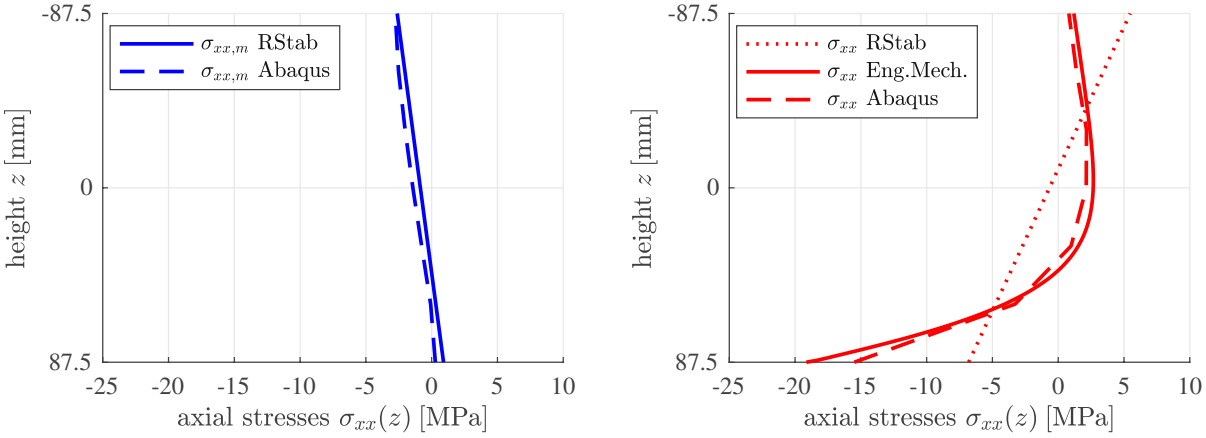

Fig. 4.16: Left wall location $x_{10} = 0.335\,\text{m}$: axial stresses of concrete **(a)** before the fire, and **(b)** half an hour after the start of the fire.

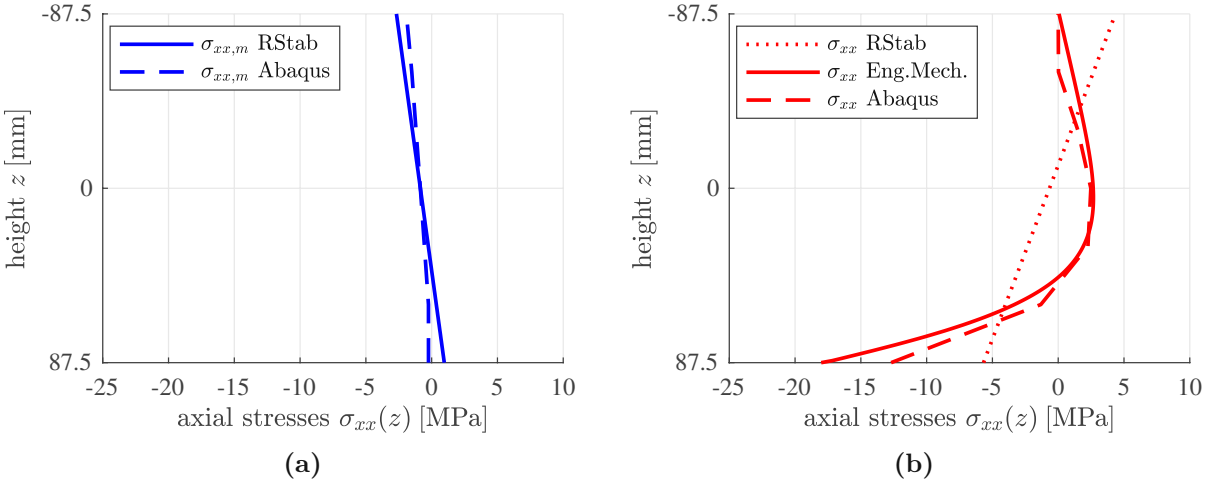

Fig. 4.17: Left wall location $x_{11} = 0.845\,\text{m}$: axial stresses of concrete **(a)** before the fire, and **(b)** half an hour after the start of the fire.

4.4.4 Left column

As for the left column, cross-sectional stresses are discussed at the position x_{12}, see Fig. 3.3. The stresses obtained with the FE simulation are well reproduced based on the engineering mechanics model, both qualitatively and quantitatively, see Fig. 4.18.

As for the situation before the fire, the stress distribution is almost constant throughout the cross-section, see Fig. 4.18a. The stress level obtained with the engineering mechanics model is virtually the same as the one obtained with the FE model. This underlines that the idealization of the prismatic column as a cylindrical one with equivalent extensional stiffness is verified for the load case referring to the point loads.

As for the time instant half an hour after the start of the fire, the total stresses agree qualitatively quite well, see Fig. 4.18b. Still, the maximum of the compressive stresses, at the outer contour of the column, is larger in the engineering mechanics analysis, and the maximum of the tensile stresses, at the center of the column, is larger in the FE analysis. One could speculate that this difference is related to the constant part of the stress distribution and, therefore, to the

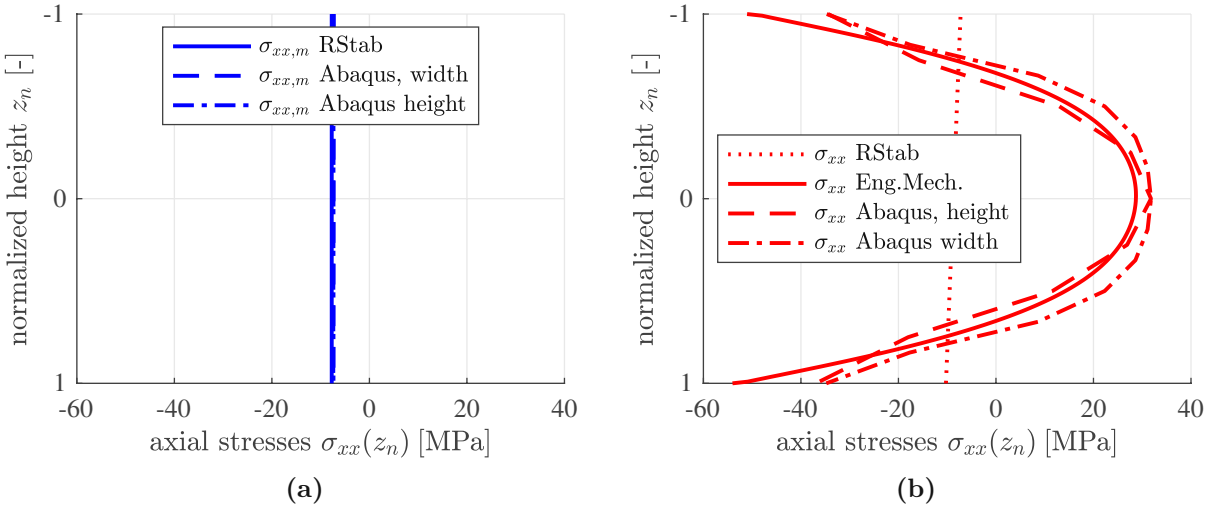

Fig. 4.18: Left column location $x_{12} = 0.845\,\text{m}$: axial stresses of concrete **(a)** before the fire, and **(b)** half an hour after the start of the fire.

axial force. In this context, it is noteworthy that the *average* temperature rise is larger in the FE model, see Fig. 4.1. Consequently, the thermal eigenstretch of the column is larger in the FE model, and this results in a compressive axial force of the column, which is larger in the FE model than in the engineering mechanics approach. This goes hand in hand with more compressive stresses and less tensile stresses in the FE model, but the opposite effect is observed in the total stress distributions, see Fig. 4.1. The reason for this nontrivial result can be explained as follows. Larger compressive axial stresses in the FE model, resulting from the larger compressive axial force, are *overcompensated* by the nonlinear part of the total stresses, i.e. by the thermal eigenstresses resulting from the prevented eigenwarping of the cross-section of the column. In this context, it is illustrative to return to the temperature changes obtained with the FE model and with the engineering mechanics model, see Fig. 4.1. The temperature *difference* between the heated lateral surface of the column and its axis is larger in the engineering mechanics analysis. Thus, the eigenwarping is larger in the engineering mechanics analysis, and thus, the self-equilibrated spatially nonlinear stress contribution is larger in the engineering mechanics model than in the FE model. These eigenstresses are compressive at the lateral surface of the column and tensile at its axis. This explains the differences between the total stresses illustrated in Fig. 4.18b.

The tensile stresses in the region around the axis of the column, obtained by means of the two used thermoelastic simulation methods, are several times larger than the characteristic tensile strength of concrete, see Fig. 4.18b. This underlines that tensile cracking of concrete in the core of the column has very likely occurred unnoticed during the fire test.

4.5 Thermo-elasto-brittle engineering analysis: tensile cracking of the core regions of the columns

In order to account for tensile failure inside the core regions of the two columns, the engineering mechanics analysis is extended towards consideration of brittle failure of concrete. To this end, it is assumed that the innermost region of the columns, with a radius amounting to 70 mm fails due to tensile cracking of concrete. As regards the extensional stiffness of the columns, the

crack-affected core region must be deactivated, causing a reduction of the effective extensional stiffness by some 34.6 %, see Table 4.2.

Tab. 4.2: Properties of the columns used for thermo-elastic analysis and for thermo-elasto-brittle analysis, respectively.

property	**without cracking**	**with cracking**
transformed cross-sectional area [mm^2]	$A_{tr} = 43871.6$	$A_{tr} = 28680.0$
extensional stiffness [kN]	$E_c A_{tr} = 1465311$	$E_c A_{tr} = 957912$
eigenstretch [10^{-4}]	$\varepsilon_0^e = 12.52$	$\varepsilon_0^e = 12.86$
axial force [kN]	$N = -383.8$	$N = -374.7$

Results of the heat conduction analysis illustrated in Fig. 4.1d remain valid, because the cracks propagate in planes orthogonal to the axis of the columns. In the material volumes between neighboring cracks, heat transfer takes place in radial direction, in an undisturbed fashion.

The spatial distribution of the thermal eigenstrains remains valid. However, the tensile eigenstrains in the cracked core region are now free to develop: they reduce the crack opening widths, but activate no stresses. Thus, the thermal eigenstrains in the cracked core region do not affect the structural behavior.

The numerical value of the eigenstretch of the columns must be updated. It is computed based on the thermal eigenstrains prevailing in the intact outer region of the columns, leading to an increased value of the eigenstretch, see Table 4.2. This can be explained as follows. The temperature in the intact outer part is, on average, higher than the average temperature of the entire cross-section. The higher average temperature goes along with an, on average, larger value of the thermal eigenstrains and, thus, a larger value of the eigenstretch, see Fig. 4.19.

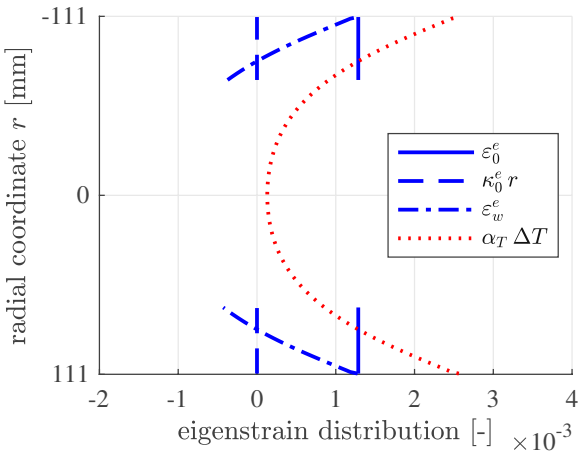

Fig. 4.19: Thermal eigenstrains of concrete half an hour after the start of the fire of the left column with consideration of tensile cracking of the core region: the dotted graph refers to total eigenstrains, the solid graph to the eigenstretch and the dash-dotted graph to the eigenwarping of the cross-section of the column.

The structural simulation based on the beam analysis software is updated. This update exclusively concerns properties of the columns; the external loads as well as the properties of the slabs and walls stay the same. The columns, in turn, have a larger thermal eigenstretch and a smaller extensional stiffness, see Table 4.2. This leads to two competing effects:

- Because of the larger thermal eigenstretch, the columns are expected to push even stronger against the top and bottom slabs. This effect tends to increase the compressive axial force carried by the columns.
- Stiffer elements of a statically indeterminate structure attract a larger share of the load than less stiff elements. Because of the reduced stiffness of the columns, this effect tends to redistribute the load towards the stiffer walls, decreasing the compressive axial force carried by the columns.

Structural analysis with the beam analysis software clarifies that the second effect slightly outperforms the former: the compressive axial force carried by the columns decreases by some 2% to −374 kN, see Table 4.2. From the viewpoint of the overall structural behavior, the redistributions of the loads, resulting from tensile cracking of the core of the columns, are rather insignificant, such that virtually the same distributions of bending moments and axial forces are obtained, compare Figs. 4.5 and 4.6 with Figs. 4.20 and 4.21.

Finally, it is interesting to discuss the stresses experienced by the intact part of the columns. Because the compressive axial force decreased slightly, and the cross-sectional area of the columns decreased significantly, see Table 4.2, the compressive axial stress due to the axial force increases relative to the simulation without consideration of tensile cracking of concrete. Still, the overall stresses remain virtually the same, because of increasing eigenstresses of the column, resulting from the prevented eigenwarping of the remaining intact cross-section of the columns, see Fig. 4.22.

It is concluded that the structural behavior is virtually unaffected by tensile cracking of the core regions of the columns. It is very likely that the columns were damaged significantly already during the first half an hour after the start of the fire, and that cracking of concrete occurred unnoticed.

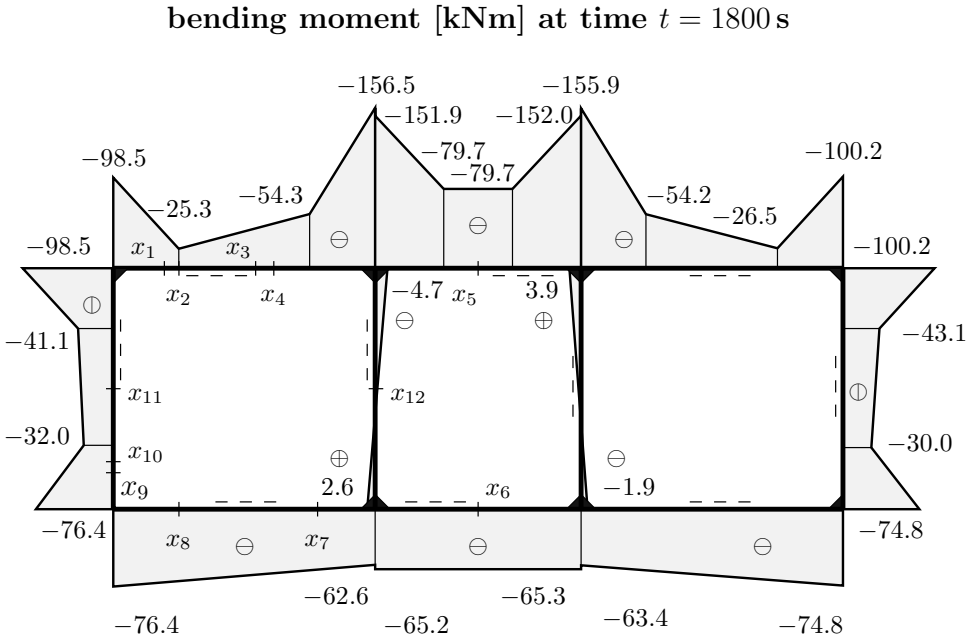

Fig. 4.20: Bending moments activated by the point loads and by fire-induced eigenstretches and eigencurvatures: simulation results obtained with RStab, under consideration of tensile cracking of the core region of the columns, see also Table 4.2.

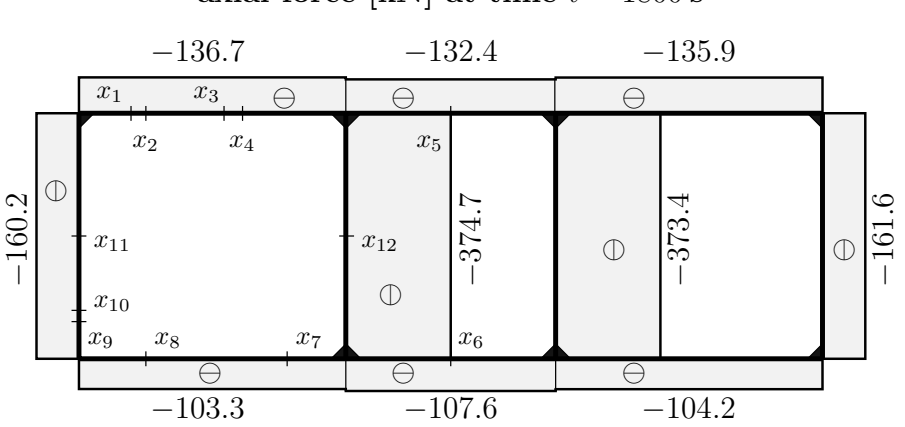

Fig. 4.21: Axial forces activated by the point loads and by fire-induced eigenstretches and eigencurvatures: simulation results obtained with RStab, under consideration of tensile cracking of the core region of the columns, see also Table 4.2.

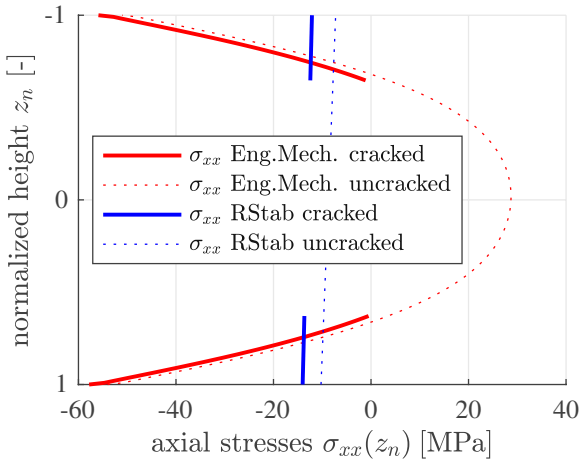

Fig. 4.22: Left column location $x_{12} = 0.845\,\text{m}$: axial stresses of concrete half an hour after the start of the fire, with and without consideration of tensile cracking of the core region.

Chapter 5

Summary and conclusions

A reinforced concrete segment of a subway station subjected, in a large-scale laboratory test [21], to ground pressure and a moderate fire, was analyzed based on an engineering mechanics model, in order to check whether or not it can reproduce the results from a linear-elastic three-dimensional Finite Element analysis [7]. The engineering mechanics model was based on the following idealizations:

- The slabs, walls, and columns of the analyzed structure were modeled by means of Euler-Bernoulli beams. The resulting frame structure consists of three cells and is statically indeterminate to the twelfth degree.
- As regards thermal loading of the slabs and walls, the transient heat conduction problems were idealized to be of one-dimensional nature: from the heated inner surfaces, in thickness direction, towards their outer surfaces. These problems were solved in a semi-analytical fashion, leading to series solutions based on trigonometric and exponential functions.
- As regards thermal loading of the columns, their rectangular cross-sections were transformed into circular cross-sections with the same extensional stiffness. This resulted in an axisymmetric heat conduction problem from the heated lateral surface, in radial direction, towards the axis of the columns. The solution of this problem was newly derived, leading to a series solution based on Bessel functions of the first kind and exponential functions.

The load carrying behavior half an hour after the start of the fire was analyzed. The engineering mechanics approach was organized as follows:

- Temperature changes relative to the uniform initial temperature were multiplied with the thermal expansion coefficients of steel and concrete, in order to quantify spatially nonlinear thermal eigenstrains in all structural elements.
- Thermal eigenstrains were subdivided, in the cross-sections of every structural element, into three parts:
  - the eigenstretch of the axis of the structural element,
  - the eigencurvature of the axis of the structural element,
  - the eigenwarping of the cross-sections of the structural element.

  This decomposition is well known for cross-sections consisting of a homogeneous material [17, 25, 31]. In the present thesis, corresponding decomposition rules were derived for *reinforced concrete* members, extending the range of applicability of the presented engineering mechanics approach. The derivation combined the Euler-Bernoulli hypothesis, geometric and constitutive equations of linear thermoelasticity, as well as standard relations between the axial force and the bending moment, on the one hand, and the axial stresses, on the other hand.

- Structural engineering-mechanics analysis was subdivided into two parts.
  - The first one referred to the larger scale of the frame structure subjected to mechanical loads simulating ground pressure as well as the thermal eigenstretches and eigencurvatures of the structural elements. This problem was solved based of the linear theory of slender straight beams, using the beam analysis software RStab. This analysis delivered distributions of axial forces and bending moments.
  - The second part referred to the smaller scale of the cross-sections where thermal eigenstresses are activated. The latter were computed from the eigenwarping-part of the thermal eigenstrains, which is prevented because the cross-sections remain plane even under combined mechanical and thermal loading. Thus, the eigenstresses can be computed by multiplying the eigenwarping-part of the eigenstrains by the negative modulus of elasticity.
- Axial stresses resulting from the two parts of the structural engineering-mechanics analysis were superimposed. The resulting stress distributions were found to agree well with axial stresses obtained from the aforementioned Finite Element simulation.

From the described thermo-elastic analysis, it was concluded that concrete cracked in the core regions of the columns, in the immediate vicinities of their axes. This was the motivation to extend the thermo-elastic analysis to a thermo-elasto-brittle analysis.

From the described analysis, several conclusions are drawn. The first set of conclusions refers to the question whether or not spatially nonlinear temperature fields, which are a characteristic of *transient* heat conduction problems, can be translated into statically equivalent linear temperature fields.

- Transient heat conduction orthogonal to the axis of a reinforced concrete beam is associated with spatially nonlinear distributions of thermal eigenstrains inside individual cross-sections. The *nonlinear* part of the eigenstrains represents an eigenwarping of the cross-sections. The latter remain plane in slender beams, even in case of transient heat conduction. This planarity is related to spatially *linear* total strains. Thus, the spatially nonlinear part of the thermal eigenstrains is prevented at the scale of the cross-sections, i.e. it is nullified by stress-related mechanical strains of identical size and distribution but opposite mathematical signs. Because the resulting thermal eigenstresses have a vanishing mean value and a vanishing first moment, they are "self-equilibrated", i.e. they do neither contribute to the axial force nor to the bending moment.
- Subtracting from the total thermal eigenstrains the nonlinear part, results in eigenstrains which are related to the thermal eigenstretch and the thermal eigencurvature of the axis of the beam analyzed. Whether eigenstretch and eigencurvature are free to develop, constrained, or prevented must be answered at the scale of the entire structure. They are free to develop in statically determinate structures. They are at least constrained in statically indeterminate structures.
- Because eigenstretches and eigencurvatures are constrained at the *larger* scale of a statically indeterminate reinforced concrete *structure*, and because the eigenwarping is prevented at the *smaller* scale of the *cross-sections*, it is impossible to translate spatially nonlinear temperature fields into statically equivalent linear temperature fields.

The second set of conclusions refers to the potential of the relatively simple (yet not trivial) engineering-mechanics approach, regarding the reproduction of results obtained with a computationally much more expensive three-dimensional Finite Element model.

- Commercially available beam analysis software is typically capable of accounting for eigenstretches and eigencurvatures. This allows for computing axial forces and bending moments as well as the related axial stresses which are linear functions within the individual cross-sections. Adding to these stress fields the spatially nonlinear thermal eigenstresses resulting from the prevented eigenwarping of the cross-sections delivers total stresses which are in good agreement with the results from the elaborate Finite Element model.

- FE analyses intrinsically suffer from a discretization error. Its quantification requires convergence analyses, i.e. the same problem must be solved based on different Finite Element meshes, and important output quantities are illustrated as a function of the discretization effort, in order to find a trade-off between discretization effort and reliability of the results obtained. Such convergence analyses require a significant amount of time, given that pre-processing of FE simulations frequently represents a large (if not the dominating) part of the time investments required for the overall analysis. The remaining discretization error manifests itself in frequently kinky rather than smooth distributions of output quantities.

- Discretization is also a topic of the developed engineering-mechanics approach, because the series solutions of the transient heat conduction problems involve infinite sums which must be truncated. Still, these series converge fast, and modern software products for numerical mathematical calculus allow for their efficient evaluation. Herein, the infinite sums were very reliably approximated based on the first 1000 summands.

- Rectangular columns were transformed into equivalent circular ones displaying the same extensional stiffness. This was beneficial, because a rather challenging two-dimensional heat conduction problem was converted into a much simpler one-dimensional one. Both the obtained distributions of temperature and axial stresses were predicted with satisfactory accuracy.

The third set of conclusions refers to lessons learned regarding the structural behavior of the analyzed segment of a subway station subjected to combined mechanical and thermal loading:

- The developed engineering mechanics approach is subdivided into a sequence of several smaller problems. This organization allows for relating causes to effects in a much more clear and intuitive fashion compared to an all-in-one simulation approach such as the Finite Element Method.

- Tensile stresses were found in all structural elements, despite the compressive loading simulating ground pressure. The locally largest tensile stresses are activated close to the axis (or the midplane) of the structural elements. Thus, tensile cracking starts *inside* the volume of the structural elements rather than visibly either at the inner or the outer surface. This renders structural inspection after non-catastrophic fire events a difficult task.

- Half an hour after the start of the fire, the columns are the most heavily stresses structural elements, because their temperature gradients were much larger than in the slabs and walls.

- Large tensile stresses were the motivation to extend the thermo-elastic approach to a thermo-elasto-brittle approach. Changes of the overall structural behavior of the frame structure, resulting from tensile cracking inside the columns, are governed by the nontrivial competition of the *increased* thermal eigenstretch and the *decreased* extensional stiffness of the columns.

- Because tensile cracking of the columns does not induce significant redistributions of the loads, tensile cracking will have occurred unnoticed in the experiment.

Overall, it is concluded that the developed mode of thermo-elastic analysis is valuable at least for pre-dimensioning purposes, because it provides interesting insight into nontrivial aspects of the structural behavior. Still, the current limitations of the presented engineering mechanics analysis shall also be addressed:

- Because a moderate fire was analyzed, mechanical properties of concrete were treated as constants and set equal to values at room temperature. In the future, these constants can be replaced by functions of temperature. Such mathematical relationships are provided by many codes for the design of reinforced concrete structures.
- The simulation with beam analysis software is based on the Euler-Bernoulli hypothesis. The latter is questionable, e.g. in the immediate vicinity of connections of different structural elements and of point loads. In order to gain detailed insight into stress distributions in such regions, Finite Element simulations appear to be indispensable.

Appendices

Appendix A

Radial heat conduction

The derivation of the solution of the radial heat conduction problem in Eq. (3.10) will be described in a step-by-step fashion in this part of the appendix. The first step is to write down the problem for cylindrical coordinates. The second step refers to the solution of the heat equation subdivided into a steady and a transient part of heat conduction. This will be done for constant initial and time-independent boundary conditions. To consider the time-dependent boundary conditions described in Chapter 3 the elementary solutions will be superimposed at the third step. At last the solutions will by verified to a column modeled with ABAQUS CAE [6].

A.1 Heat conduction specified for cylindrical coordinates

Rewriting the general form of the heat conduction problem in case of isotropic heat conduction properties from Eq. (3.2) reads as

$$\dot{T} - a\,\nabla \cdot (\boldsymbol{I} \cdot \nabla T) = 0\,. \tag{A.1}$$

Herein, a denotes the thermal diffusivity, $\boldsymbol{I} = \sum_{i=1}^{3} \underline{e}_i \otimes \underline{e}_i$ denotes the second order identity tensor, $T = T(\underline{x})$ denotes the temperature distribution, and ∇ denotes the nabla operator for cylindrical coordinates (r,φ,z). The transposed nabla operator ∇^T is defined as

$$\nabla^T = \left[\; \frac{\partial}{\partial r}\,,\quad \frac{1}{r}\frac{\partial}{\partial \varphi}\,,\quad \frac{\partial}{\partial z}\;\right]. \tag{A.2}$$

Inserting Eq. (A.2) into Eq. (A.1) yields the general form of the heat conduction problem for a cylindrical coordinate system, as

$$\begin{aligned}\frac{\partial T}{\partial t} &= a\left[\frac{1}{r}\frac{\partial}{\partial r}\left(r\,\frac{\partial T}{\partial r}\right) + \frac{1}{r}\frac{\partial}{\partial \varphi}\left(\frac{1}{r}\frac{\partial T}{\partial \varphi}\right) + \frac{\partial}{\partial z}\left(\frac{\partial T}{\partial z}\right)\right],\\ &= a\left(\frac{\partial^2 T}{\partial r^2} + \frac{1}{r}\frac{\partial T}{\partial r} + \frac{1}{r^2}\frac{\partial^2 T}{\partial \varphi^2} + \frac{\partial^2 T}{\partial z^2}\right).\end{aligned} \tag{A.3}$$

In Eq. (A.3) the expression on the right side of the equal sign represents the spatial distribution heat flux. In case of heat conduction only in radial direction, the heat flux which depends only on the directions φ and z is equal to zero. Thus, the radial heat conduction problem with temperature $T = T(r,t)$ reads as

$$\frac{\partial T}{\partial t} = a\left(\frac{\partial^2 T}{\partial r^2} + \frac{1}{r}\frac{\partial T}{\partial r}\right). \tag{A.4}$$

A.2 Semi-analytical solution for radial heat conduction

The derivation of the solution of the radial heat conduction problem in Eq. (A.4) refers to a circular cross-section with radius R. At the beginning ($t = 0$) the temperature is equal to the reference temperature T_{ref} at the whole cross section. At the lateral surface a time-independent temperature T^{lat} is prescribed. In this case the initial condition and the boundary condition for one temperature step can be written as:

$$T(r, t = 0) = T_{ref} \qquad \text{initial condition,} \tag{A.5}$$

$$T(r = R, t) = T^{lat} \qquad \text{constant boundary condition at the surface for one increment.} \tag{A.6}$$

Because of the linearity of the partial differential equation (A.4) the superposition principle applies. Thus, the solution of the heat equation can be subdivided into two subproblems. The first subproblem (index s) refers to the steady part and the second subproblem (index t) refers to the transient part of the heat equation. Superposition of both parts yields the total temperature distribution in radial direction $T = T_s + T_t$. Specializing Eq. (A.4) for the steady part of heat conduction reads as

$$\frac{\partial T_s}{\partial t} = a \left(\frac{\partial^2 T_s}{\partial r^2} + \frac{1}{r} \frac{\partial T_s}{\partial r} \right) \qquad \text{with} \qquad \frac{\partial T_s}{\partial t} = 0 \,. \tag{A.7}$$

Eq. A.7 can be integrated in two steps as described in literature [16]. This leads to

$$\text{Step 1:} \qquad \frac{1}{r} \frac{\partial}{\partial r} \left(r \frac{\partial T_s}{\partial r} \right) = 0 \qquad \Rightarrow \underbrace{\int \frac{\partial}{\partial r} \left(r \frac{\partial T_s}{\partial r} \right) \mathrm{d}r}_{r \cdot \frac{\partial T_s}{\partial r}} = A,$$

$$\text{Step 2:} \qquad \int \frac{\partial T_s}{\partial r} \mathrm{d}r = \int A \frac{1}{r} \, \mathrm{d}r \,, \qquad \Rightarrow T_s = A \, ln(r) + B \,. \tag{A.8}$$

where A and B denote the integration constants. This solution can be valid for solid cylinders only if the coefficient A is equal to zero. Inserting the boundary condition in Eq. (A.6) into the result from Eq. (A.8) yields the steady part of the radial heat conduction problem as $T_s = B = T^{lat}$. Considering Eqs. (A.5) and (A.6) in addition to the steady part of the heat conduction problem leads to the the initial condition and boundary condition of the the second subproblem, which reads as

$$\left\{ \begin{array}{c} T(r,t) \\ T(r, t = 0) = T_{ref} \\ T(r = R, t) = T^{lat} \end{array} \right\} = \left\{ \begin{array}{ccc} T_s & + & T_t \\ T^{lat} & + & T_{ref} - T^{lat} \\ T^{lat} & + & 0 \end{array} \right\} . \tag{A.9}$$

The second subproblem denoting a transient heat conduction problem given in Eq. (A.4) will be solved by using the technique of separation of variables for partial differential equations:

$$T_t(r, t) = f(r) \, g(t) \,. \tag{A.10}$$

Inserting Eq. (A.10) into Eq. (A.4) and moving terms depending on t to the left side of the equal sign and terms depending on r to the right side leads to

$$\frac{\frac{\mathrm{d}g(t)}{\mathrm{d}t}}{ag(t)} = \frac{\frac{\mathrm{d}^2f(r)}{\mathrm{d}r^2} + \frac{1}{r}\frac{\mathrm{d}f(r)}{\mathrm{d}r}}{f(r)} = -\lambda^2 \rightarrow \left\{ \begin{array}{c} \frac{\mathrm{d}g(t)}{\mathrm{d}t} + a\lambda^2 g(t) = 0 \\ \frac{\mathrm{d}^2f(r)}{\mathrm{d}r^2} + \frac{1}{r}\frac{\mathrm{d}f(r)}{\mathrm{d}r} + \lambda^2 f(r) = 0 \end{array} \right\}. \tag{A.11}$$

Herein, λ denotes the eigenvalue of the field equation and will be defined subsequently. The time-dependent differential equation in Eq. (A.11) will be solved by formulating exponential laws. This yields

$$g(t) = \hat{A}\,\exp(-\lambda^2 a t)\,, \tag{A.12}$$

where $\hat{A}$ denotes a auxiliary coefficient. The spatial-dependent expression in Eq. (A.11) denotes a partial differential equation with variable coefficients, also known as Bessel's differential equation [16].

Excursus: Bessel's differential equations

The general form of Bessel's differential equation is based on classical Sturm–Liouville theory and reads as

$$x^2\frac{\mathrm{d}^2f(x)}{\mathrm{d}x^2} + x\frac{\mathrm{d}f(x)}{\mathrm{d}x} + (x^2-\nu^2)f(x) = 0 \quad \forall\,\nu \in \mathbb{R}\,. \tag{A.13}$$

Herein, x denotes the argument and ν denotes the order of Bessel's differential equation. The solution of Eq. (A.13) can be gained with infinite power series with coefficients a_k:

$$f(x) = x^\nu \sum_{k=0}^{\infty} a_k\, x^k. \tag{A.14}$$

Inserting the expression of the power series in Eq. (A.14) into Eq. (A.13) leads to the solution of Bessels' differential equation, also known as the Bessel function of the first kind $J_\nu(x)$ with order ν. This reads as

$$J_\nu(x) = \left(\frac{x}{2}\right)^\nu \sum_{k=0}^{\infty} \frac{(-1)^k}{\Gamma(k+1)\,\Gamma(\nu+k+1)} \left(\frac{x}{2}\right)^{2k}. \tag{A.15}$$

Herein, Γ denotes the Gamma function, which is necessary to define the solution to all $\nu \in \mathbb{R}$. It is noteworthy at this point that the coefficients a_k are uniformly convergent. Due to the classical Sturm–Liouville theory the eigenvalues of the Bessel function of the first kind $J_\nu(x)$ have the following characteristics:

- All eigenvalues are real.
- Eigenfunctions of different eigenvalues are orthogonal.
- For each eigenvalue there is only one linearly independent eigenfunction.

In order to create a fundamental system for total solution of Bessel's differential equation, the Bessel function of the second kind $Y_\nu(x)$ has to be introduced in consideration of the verification of linear independence:

$$Y_\nu(x) = \frac{\cos(\nu\pi)\,J_\nu(x) - J_{-\nu}(x)}{\sin(\nu\pi)}\,. \tag{A.16}$$

The total solution of Bessel's differential equation is defined as the linear combination of the Bessel function of the first kind (see Eq. (A.15)) and the Bessel function of the second kind (see Eq. (A.16)). This reads as

$$f(x) = A\,J_\nu(x) + B\,Y_\nu(x)\,. \tag{A.17}$$

Expanding the spatial-dependent expression of Eq. (A.11) with r^2 yields

$$r^2\frac{\mathrm{d}^2 f(r)}{\mathrm{d}r^2} + r\,\frac{\mathrm{d}f(r)}{\mathrm{d}r} + (\lambda r)^2 f(r) = 0\,. \tag{A.18}$$

This expression is equal to Bessel's differential equation of zeroth-order, see Eq. (A.13). Thus, the total solution is gained in consideration to Eq. (A.18) as

$$f(r) = \tilde{A}\,J_0(\lambda r) + \tilde{B}\,Y_0(\lambda r)\,, \tag{A.19}$$

where $J_0(\lambda\,r)$ denotes the zeroth-order Bessel function of the first kind, and $Y_0(\lambda\,r)$ denotes the zeroth-order Bessel function of the second kind. $\tilde{A}$ and $\tilde{B}$ are auxiliary coefficients. Because second kind Bessel function is unrestricted at the origin with $Y_0(0) \to -\infty$, the coefficient $\tilde{B}$ has to be equal to zero to create a solution for the temperature distribution of the whole cross-section. Inserting the separated solutions in Eqs. (A.12) and (A.19) into Eq. (A.10) yields

$$T_t(r,t) = A\,\exp(-\lambda^2 at) J_0(\lambda r)\,, \tag{A.20}$$

where $A = \hat{A}\,\tilde{A}$ is the total coefficient of the solution that will be quantified by specializing Eq. (A.20) for the boundary condition. Inserting the boundary condition in Eq. (A.9) into Eq. (A.20) yields

$$T_t(r=R,t) = A\,\underbrace{\exp(-\lambda^2 at)}_{\neq 0}\,J_0(\lambda R) = 0. \tag{A.21}$$

The expression has to be valid for each time t, also for $t = 0$. Because of this there are two cases that will be possible to fulfill the equal sign. The first one will create the trivial solution with A is equal to zero. The second one leads to the eigenvalue problem that reads as

$$J_0(\lambda R) = J_0(\alpha_n) = 0 \qquad \text{with} \qquad \alpha_n = \lambda_n R \quad \Rightarrow \quad \lambda_n = \frac{\alpha_n}{R}\,. \tag{A.22}$$

Herein, α_n are the eigenvalues of the general Bessel function of the first kind with $n \in \mathbb{N} \setminus \{0\}$. This eigenvalues can not be determined in an analytical way. Thus, the eigenvalues will be calculated using an iterative numerical procedure, see Fig. A.1. In order to determine the eigenvalues of the present heat conduction problem the general eigenvalues α_n will be scaled by the radius R of the cross-section as defined in Eq. (A.22). If an infinite number of coefficients A_n exist, which satisfy the boundary conditions, the solution of the transient heat conduction problem can be written as infinite series of sub-solutions:

$$T_t(r,t) = \sum_{n=1}^{\infty} A_n\,\exp(-\lambda_n^2 at) J_0(\lambda_n r)\,. \tag{A.23}$$

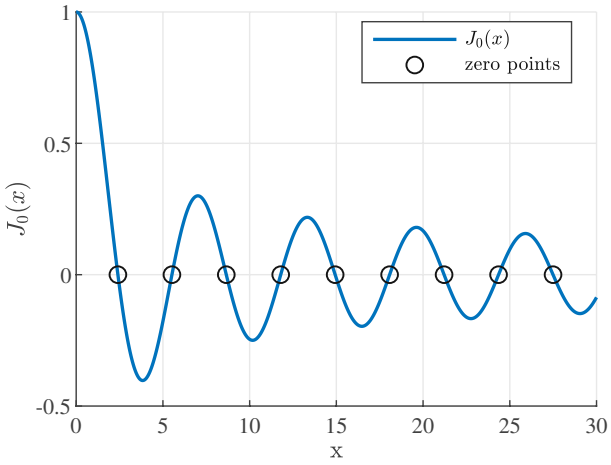

α_n
$\alpha_1 = 2{,}4048$
$\alpha_2 = 5{,}5201$
$\alpha_3 = 8{,}6537$
$\alpha_4 = 11{,}7915$
$\alpha_5 = 14{,}9309$
$\alpha_6 = 18{,}0711$
$\alpha_7 = 21{,}2116$
$\alpha_8 = 24{,}3525$
$\alpha_9 = 27{,}4935$
...

Fig. A.1: Values of the first nine zero points α_n of the general zeroth-order Bessel function of the first kind with $J_0(x)$.

Specializing Eq. (A.23) for the initial condition in Eq. (A.9) leads to an expression for determining the coefficients A_n. This reads as

$$T_t(r, t=0) = \sum_{n=1}^{\infty} A_n J_0(\lambda_n r) = T_{ref} - T^{lat} \,. \tag{A.24}$$

Eq. (A.24) will be extended with $J_0(\lambda_m r)\, r$ and $m \in \mathbb{N} \setminus \{0\}$, and integrated over the radial direction with limits from zero to R. If A_n is convergent the sum sign and the integration sign will change positions. All this leads to

$$\sum_{n=1}^{\infty} A_n \int_0^R J_0(\lambda_n r)\, J_0(\lambda_m r)\, r \,\mathrm{d}r = (T_{ref} - T^{lat}) \int_0^R r\, J_0(\lambda_m r) \,\mathrm{d}r \,. \tag{A.25}$$

The integral on the left side of the equation sign denotes a dot product of two functions. Specializing this for the cases $m = n$ and $m \neq n$ yields

$$\langle J_0(\lambda_n r), J_0(\lambda_m r) \rangle = \int_0^R J_0(\lambda_n r)\, J_0(\lambda_m r)\, r \,\mathrm{d}r = \begin{cases} \frac{R^2 \cdot (J_0^2(\lambda_n R) + J_1^2(\lambda_n R))}{2} & \text{for} \quad m = n \,, \\ 0 & \text{for} \quad m \neq n \,. \end{cases} \tag{A.26}$$

Because of the orthogonality of the Bessel functions of the first kind the dot product in case $m \neq n$ is equal to zero. Thus, the integral on the right side of the equation sign is re-written for $m = n$:

$$\int_0^R r \cdot J_0(\lambda_n r) \,\mathrm{d}r = \frac{R \cdot J_1(\lambda_n R)}{\lambda_n} \,. \tag{A.27}$$

Inserting Eqs. (A.26) and (A.27) into Eq. (A.26) and specializing for a single coefficient A_n leads to

$$A_n = \frac{2\,(T_{ref} - T^{lat})}{R} \frac{1}{J_1(\lambda_n R)\, \lambda_n} \,. \tag{A.28}$$

Thus, the solution of the transient heat conduction can be written as

$$T_t(r,t) = \frac{2\,(T_{ref} - T^{lat})}{R} \sum_{n=1}^{\infty} \frac{1}{J_1(\lambda_n R)\,\lambda_n} J_0(\lambda_n r)\, \exp(-\lambda_n^2 a t)\,. \tag{A.29}$$

The temperature distribution including the steady part (A.8) and the transient part (A.29) reads as

$$T(r,t) = T_s + T_t(r,t) = T^{lat} + \frac{2\,(T_{ref} - T^{lat})}{R} \sum_{n=1}^{\infty} \frac{1}{J_1(\lambda_n R)\,\lambda_n} J_0(\lambda_n r)\, \exp(-\lambda_n^2 a t)\,. \tag{A.30}$$

Rearranging the expressions in Eq. (A.30) considering the general eigenvalues of the Bessel function of the first kind in Eq. (A.22) leads to a generalized temperature distribution, see Fig. A.2. This reads as

$$\frac{T(r,t) - T^{lat}}{T_{ref} - T^{lat}} = 2 \sum_{n=1}^{\infty} \frac{J_0(\alpha_n \frac{r}{R})}{J_1(\alpha_n)\,\alpha_n} \exp(-\alpha_n^2 \tau) = f\left(\frac{r}{R}, \tau = \frac{at}{R^2}\right)\,. \tag{A.31}$$

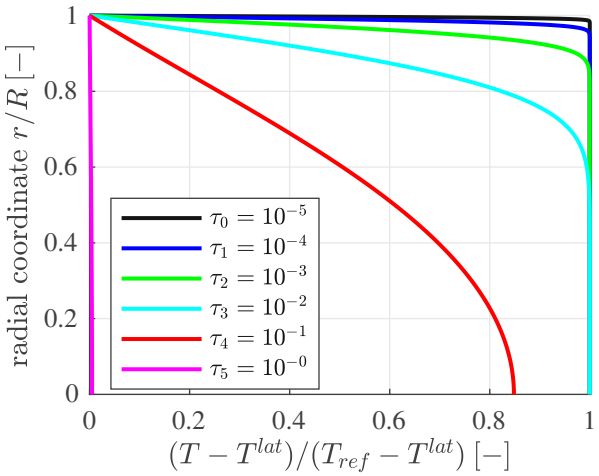

Fig. A.2: Generalized temperature distribution plotted at several times τ; Due to the symmetry only the positive radial coordinates are displayed;In Eq. (A.31) 1000 terms were considered.

A.3 Semi-analytical solution for finite temperature steps

Due to the linearity of the heat conduction problem described in Eq. (A.1) the superposition principle applies. Thus, the elementary solutions derived for one temperature increment will superimposed for a finite number of temperature steps N_T. Therefore, the amount of the boundary condition for one increment has to be defined as follows:

$$\Delta T_k^{lat} = T_k^{lat} - T_{k-1}^{lat}. \tag{A.32}$$

Herein, T_k^{lat} denotes the present increment and T_{k-1}^{lat} denotes the increment before with $k = 1, 2, \ldots, N_T$. The temperature at T_0^{lat} is equal to the reference temperature T_{ref}. Superimposing the temperature distribution in Eq. (A.30) for N_T increments yields

$$T(r,t) = \sum_{k=1}^{N_T} T_k(r,t) = T^{lat} + \sum_{k=1}^{N_T} \frac{2\,(T_{ref} - \Delta T_k^{lat})}{R} \sum_{n=1}^{\infty} \frac{J_0(\lambda_n r)}{J_1(\lambda_n R)\,\lambda_n} \exp(-\lambda_n^2 a \langle t - t_k \rangle)\,. \quad \text{(A.33)}$$

This is the semi-analytical solution of radial heat conduction. The expression in the angled brackets denotes the Macauley operator defined in Eq. (3.9).

A.4 Code-verification with results from ABAQUS CAE

The semi-analytical solution of the radial heat conduction problem was verified by using ABAQUS CAE [6]. Therefore, a cylindrical column with uniform boundary conditions in temperature was simulated at several times during the heating, see Fig. A.3 and Fig. A.4. Thus, the correctness of the solution was confirmed by comparing the temperature distributions.

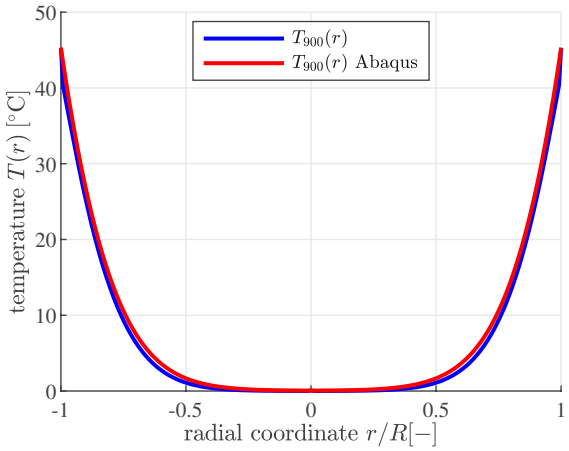

Fig. A.3: Code verification for temperature distribution $T(r,t)$ at time $t = 900$ s with 15 temperature increments; The steady and transient part of heat conduction are included.

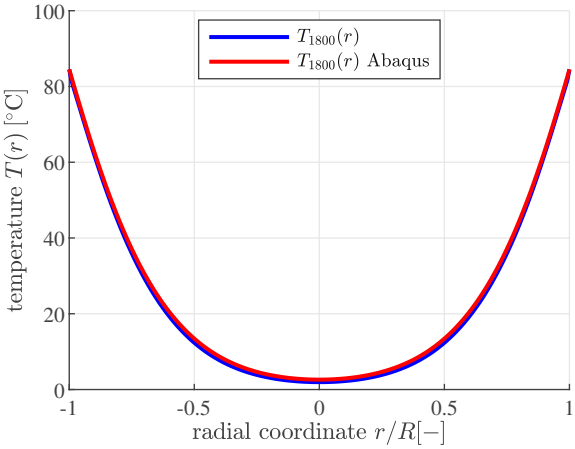

Fig. A.4: Code verification for temperature distribution $T(r,t)$ at time $t = 1800$ s with 30 temperature increments; The steady and transient part of heat conduction are included.

Appendix B

Thermal stresses of radial symmetric reinforced concrete cross-sections

The thermal eigenstrains, ε^e, developed at the points r and φ inside the cross-section of a cylindrical column, see Fig. 3.2, are equal to the thermal expansion coefficient evaluated at those points, $\alpha_T = \alpha_T(r, \varphi)$, multiplied with the change of temperature, measured relative to the reference configuration, $\Delta T(r, t) = T(r, t) - T_{ref}$, as:

$$\varepsilon^e_{xx} = \varepsilon^e_{rr} = \varepsilon^e_{\varphi\varphi} = \alpha_T \Delta T \,. \tag{B.1}$$

In a transient heat conduction problem, the thermal eigenstrains are spatially nonlinear along the thickness direction, see e.g., [17, 25, 31]. When it comes to the quantification of thermal stresses, it must be determined whether the eigenstrains are free to develop, constrained, or prevented. This is determined partly at the larger, structural level, and partly at the smaller cross-sectional level. To this end, the spatially nonlinear eigenstrains are subdivided into three parts. They refer to an eigenstretch of the column, an eigencurvature of the column, and an eigenwarping of the cross-section. The eigenstretch and the eigencurvature of the axis of the column cause axial stresses depending on the boundary conditions that constrain the deformation of the structure. On the other hand, the assumption that plane sections remain plane means that the eigenwarping of the cross-section of the column is prevented, thus always resulting in nonlinear thermal stresses. Herein, we focus on radial-symmetric cross-sections with non-uniform modulus of elasticity and thermal expansion coefficient, E and α_T, respectively, assuming a cylindrical coordinate system with origin at the axis of the column, see Fig. 3.2. The transformation of the Cartesian coordinate system used for the derivation in Section 3.2 into cylindrical coordinates reads as

$$\begin{aligned} y &= r\,\cos(\varphi)\,, \\ z &= r\,\sin(\varphi)\,, \\ \mathrm{d}A &= \mathrm{d}y\mathrm{d}z = r\;\mathrm{d}r\mathrm{d}\varphi\,. \end{aligned} \tag{B.2}$$

This yields

$$\int_A E\,z\;\mathrm{d}A = \int_A E\,r\,\cos(\varphi)\;\mathrm{d}A = 0 \tag{B.3}$$

The first step refers to the kinematics of the Euler-Bernoulli theory for slender beams transformed into cylindrical coordinates:

$$u = u_0 - \frac{\partial w_0}{\partial x}\,z = u_0 - \frac{\partial w_0}{\partial x}\,r\,\sin(\varphi)\,, \tag{B.4}$$

where u denotes the displacement components in x-direction, at any point within the volume of the column. u_0 and w_0 denote the displacement components at the axis of the column. Eq. (B.4) essentially describes that cross-sections remain plane and normal to the deformed axis of the beam, also in the deformed configuration (= Euler-Bernoulli hypothesis).

The second step refers to ("total") axial strain component ε_{xx} of the linearized strain tensor. It is defined as

$$\varepsilon_{xx} = \frac{\partial u}{\partial x}\,. \tag{B.5}$$

Inserting Eq. (B.4) into Eq. (B.5) yields

$$\varepsilon_{xx} = \frac{\partial u_0}{\partial x} - \frac{\partial^2 w_0}{\partial x^2}\, r\, \sin(\varphi)\,. \tag{B.6}$$

Eq. (B.6) is usually reformulated in terms of the stretch of the axis of the column, $\varepsilon_0 = \partial u_0/\partial x$, and its curvature, $\kappa_0 = -\partial^2 w_0/\partial x^2$. This yields

$$\varepsilon_{xx} = \varepsilon_0 + \kappa_0\, r\, \sin(\varphi)\,. \tag{B.7}$$

The third step refers to axial stress component σ_{xx} of Cauchy's stress tensor. In thermoelasticity, it reads as

$$\sigma_{xx} = E\,(\varepsilon_{xx} - \varepsilon^e_{xx})\,. \tag{B.8}$$

Inserting Eqs. (B.1) and (B.7) into (B.8) yields

$$\sigma_{xx} = E\,(\varepsilon_0 + \kappa_0\, r\, \sin(\varphi) - \alpha_T \Delta T)\,. \tag{B.9}$$

where the modulus of elasticity is a function of the r- and φ-coordinates which describe points inside the cross-sections of the column, i.e. $E = E(r, \varphi)$.

The fourth step refers to axial force N. It is energetically conjugate to the displacements u_0 and read as

$$N = \int_A \sigma_{xx}\, \mathrm{d}A\,. \tag{B.10}$$

Inserting Eq. (B.9) into (B.10) yields under consideration of (B.3):

$$\begin{aligned} N &= \int_A E\,(\varepsilon_0 + \kappa_0\, r\, \sin(\varphi) - \alpha_T \Delta T)\, \mathrm{d}A\,, \\ &= \underbrace{\int_A E\, \mathrm{d}A}_{\overline{EA}}\, \varepsilon_0 - \underbrace{\int_A E\, \alpha_T \Delta T\, \mathrm{d}A}_{\overline{EA}\,\varepsilon^e_0}\,, \\ &= \overline{EA}(\varepsilon_0 - \varepsilon^e_0)\,. \end{aligned} \tag{B.11}$$

Eq. (B.11) is the motivation to introduce the effective extensional stiffness of the column as

$$\overline{EA} = \int_A E\, \mathrm{d}A\,. \tag{B.12}$$

In the case of a reinforced concrete columns, $\overline{EA}$ can be rewritten as

$$\int_A E\, \mathrm{d}A = \int_{A_c} E_c\, \mathrm{d}A + \int_{A_s} E_s\, \mathrm{d}A = E_c A_c + E_c \underbrace{\frac{E_s}{E_c}}_{n_E} \sum_{j=1}^{L} A_{s,j} = E_c \underbrace{\left[A_c + n_E \sum_{j=1}^{L} A_{s,j}\right]}_{A_{tr}}\,, \tag{B.13}$$

where n_E refers to the ratio between the modulus of elasticity of steel, E_s, and concrete, E_c, j refers to each one of the L individual steel reinforcement bars existing within the cross-section, and $A_{tr} = A_c + n_E \sum_{j=1}^{L} A_s$ refers to the total area of the "transformed" section with A_c denotes the area of concrete and A_s denotes the area of steel. Thus, one can conclude from Eq. (B.11) that the eigenstretch of the axis of the column is calculated as

$$\varepsilon_0^e = \frac{1}{\overline{EA}} \int_A E\,\alpha_T \Delta T \; \mathrm{d}A\,, \tag{B.14}$$

which in case of a concrete column that presents a constant temperature in each reinforcement bar, considering Eqs. (3.24) and (3.25), leads to

$$\begin{aligned}
\varepsilon_0^e &= \frac{1}{\overline{EA}} \left[\int_{A_c} E_c\,\alpha_{T,c}\,\Delta T \; \mathrm{d}A + \sum_{j=1}^{L} E_s\,\alpha_{T,s}\,\Delta T_j\,A_{s,j} \right], \\
&= \frac{1}{E_c\,A_{tr}} E_c \left[\int_{A_c} \alpha_{T,c}\,\Delta T \; \mathrm{d}A + n_E \sum_{j=1}^{L} \alpha_{T,s}\,\Delta T_j\,A_{s,j} \right], \\
&= \frac{1}{A_{tr}} \left[\alpha_{T,c} \int_{A_c} \Delta T \; \mathrm{d}A + n_E \sum_{j=1}^{L} \alpha_{T,s}\,\Delta T_j\,A_{s,j} \right],
\end{aligned} \tag{B.15}$$

where $\alpha_{T,c}$ is the thermal expansion of concrete and $\alpha_{T,s}$ is the thermal expansion of steel. In the case of uniform heating at the lateral surface of the column as described in Appendix A under consideration of the definition of temperature changes ΔT the integral in Eq. (B.15) leads to:

$$\begin{aligned}
\int_{A_c} \Delta T \; \mathrm{d}A &= \int_{A_c} \Delta T^{lat} + \sum_{k=1}^{N_T} \frac{2(T_{ref} - \Delta T_k^{lat})}{R} \sum_{n=1}^{\infty} \underbrace{\frac{1}{J_1(\lambda_n R)\lambda_n}}_{A_n} J_0(\lambda_n r) \exp(-\lambda_n^2 a \langle t - t_k \rangle) \; \mathrm{d}A, \\
&= \Delta T^{lat} \underbrace{\int_{A_c} \mathrm{d}A}_{A_c} + \sum_{k=1}^{N_T} \frac{2(T_{ref} - \Delta T_k^{lat})}{R} \sum_{n=1}^{\infty} A_n \exp(-\lambda_n^2 a \langle t - t_k \rangle) \int_{A_c} J_0(\lambda_n r) \mathrm{d}A, \\
&= \Delta T_{hot,k}\,A_c + \sum_{k=1}^{N_T} \frac{2(T_{ref} - \Delta T_k^{lat})}{R} \sum_{n=1}^{\infty} A_n \exp(-\lambda_n^2 a \langle t - t_k \rangle) \underbrace{\int_0^{2\pi} \int_0^{R} J_0(\lambda_n r)\, r \; \mathrm{d}r \mathrm{d}\varphi}_{\frac{2\,R\,\pi\,J_1(\lambda_n R)}{\lambda_n}}, \\
&= A_c \left[\Delta T^{lat} + \sum_{k=1}^{N_T} \frac{4(T_{ref} - \Delta T_k^{lat})}{R^2} \sum_{n=1}^{\infty} \frac{1}{\lambda_n^2} \exp(-\lambda_n^2 a \langle t - t_k \rangle) \right].
\end{aligned} \tag{B.16}$$

Inserting Eq. (B.16) into Eq. (B.15) leads to the eigenstretch of the radial-symmetric reinforced concrete column, read as

$$\varepsilon_0^e = \alpha_{T,c}\frac{A_c}{A_{tr}}\left[\Delta T^{lat} + \sum_{k=1}^{N_T}\frac{4(T_{ref}-\Delta T_k^{lat})}{R^2}\sum_{n=1}^{\infty}\frac{1}{\lambda_n^2}\exp(-\lambda_n^2 a\langle t-t_k\rangle)\right] \tag{B.17}$$
$$+\, n_E\,\alpha_{T,s}\sum_{j}^{L}\frac{A_{s,j}}{A_{tr}}\Delta T_j\,.$$

The fifth step refers to bending moment M. It is energetically conjugate to the cross-sectional rotation $\partial w_0/\partial x$ and reads as

$$M = \int_A \sigma_{xx}\, z\, \mathrm{d}A = \int_A \sigma_{xx}\, r\, \sin(\varphi)\, \mathrm{d}A\,, \tag{B.18}$$

Inserting Eq. (B.9) into (B.18) yields under consideration of (B.3):

$$\begin{aligned} M &= \int_A E\left(\varepsilon_0 + \kappa_0\, r\, \sin(\varphi) - \alpha_T\Delta T\right) r\, \sin(\varphi)\, \mathrm{d}A\,, \\ &= \underbrace{\int_A E\, r^2\, \sin^2(\varphi)\, \mathrm{d}A}_{\overline{EI}}\,\kappa_0 - \underbrace{\int_A E\,\alpha_T\Delta T\, r\, \sin(\varphi)\, \mathrm{d}A}_{\overline{EI}\,\kappa_0^e}\,, \\ &= \overline{EI}(\kappa_0 - \kappa_0^e)\,. \end{aligned} \tag{B.19}$$

Eq. (B.19) is the motivation to introduce the effective bending stiffness of the column as

$$\overline{EI} = \int_A E\, r^2\, \sin^2(\varphi)\, \mathrm{d}A\,. \tag{B.20}$$

In the case of a reinforced concrete column, $\overline{EI}$ can be rewritten as

$$\begin{aligned} \int_A E\, r^2\, \sin^2(\varphi)\, \mathrm{d}A &= \int_{A_c} E_c\, r^2\, \sin^2(\varphi)\, \mathrm{d}A + \int_{A_s} E_s\, r^2\, \sin^2(\varphi)\, \mathrm{d}A\,, \\ &= E_c I_c + E_c\,\underbrace{\frac{E_s}{E_c}}_{n_E}\sum_{j=1}^{L} A_{s,j}\, r_{s,j}^2\, \sin^2(\varphi)\,, \qquad \text{(B.21)} \\ &= E_c\underbrace{\left[I_c + n_E\sum_{j=1}^{L} A_{s,j}\, r_{s,j}^2\, \sin^2(\varphi)\right]}_{I_{tr}}\,, \qquad \text{(B.22)} \end{aligned}$$

where $I_{tr} = I_c + n_E\,\sum_{j=1}^{L} A_{s,j}\, r_{s,j}^2\, \sin^2(\varphi)$ refers to the second moment of inertia of the "transformed" cross section, φ denotes the reference axis for parallel axis theorem, and $r_{s,j}$ refers to the distance between each individual reinforcement bar/layer and the reference axis. The eigencurvature of the axis of the column is calculated according to Eq. (B.19) as

$$\kappa_0^e = \frac{1}{\overline{EI}}\int_A E\,\alpha_T\Delta T\, r\, \sin(\varphi)\, \mathrm{d}A\,. \tag{B.23}$$

which in the case of a reinforced concrete column that presents a constant temperature within each reinforcement bar, considering Eqs. (B.22) and (B.23), leads to

$$\begin{aligned}\kappa_0^e &= \frac{1}{\overline{EI}}\left[\int_{A_c} E_c\,\alpha_{T,c}\,\Delta T\,r\,\sin(\varphi)\;\mathrm{d}A + \sum_{j=1}^{L} E_s\,\alpha_{T,s}\,\Delta T_j\,A_{s,j}\,r_{s,j}^2\,\sin^2(\varphi)\right],\\ &= \frac{1}{E_c\,I_{tr}}E_c\left[\int_{A_c} \alpha_{T,c}\,\Delta T\,r\,\sin(\varphi)\;\mathrm{d}A + n_E\sum_{j=1}^{L} \alpha_{T,s}\,\Delta T_j\,A_{s,j}\,r_{s,j}^2\,\sin^2(\varphi)\right],\\ &= \frac{1}{I_{tr}}\left[\int_{A_c} \alpha_{T,c}\,\Delta T\,r\,\sin(\varphi)\;\mathrm{d}A + n_E\sum_{j=1}^{L} \alpha_{T,s}\,\Delta T_j\,A_{s,j}\,r_{s,j}^2\,\sin^2(\varphi)\right]. \qquad \text{(B.24)}\end{aligned}$$

According to the symmetry of the radial heat conduction problem described in Appendix A and the uniform temperature at the lateral surface of the column the eigencurvature of the axis, κ_0^e, is equal to zero. Thus, the completed derivation underlines that the spatially nonlinear eigenstrain distribution, $\alpha_T\Delta T$, of columns with uniform heating at the lateral surface can be decomposed into two contributions:

$$\alpha_T\Delta T = \varepsilon_0^e + \varepsilon_w^e\,, \qquad \text{(B.25)}$$

In Eq. (B.25), ε_0^e denotes a spatially constant contribution according to Eq. (B.14), representing an eigenstretch of the beam; and ε_w^e denotes the spatially non-linear rest of the eigenstrain distribution, representing an eigenwarping of the cross-section of the beam.

Thermal stresses are derived as follows: Under consideration of $\kappa_0^e = 0$, Eqs. (B.11) and (B.19) are rearranged as

$$\varepsilon_0 = \frac{N}{\overline{EA}} + \varepsilon_0^e\,, \qquad \text{(B.26)}$$

$$\kappa_0 = \frac{M}{\overline{EI}}\,. \qquad \text{(B.27)}$$

Inserting Eqs. (B.26) and (B.27) into Eq. (B.9) yields

$$\begin{aligned}\sigma_{xx}(r,\varphi) &= E(r,\varphi)\left[\left(\frac{N}{\overline{EA}} + \varepsilon_0^e\right) + \frac{M}{\overline{EI}}\,r\,\sin(\varphi) - \alpha_T(r,\varphi)\,\Delta T(r)\right]\\ &= \frac{N\,E(r,\varphi)}{\overline{EA}} + \frac{M\,E(r,\varphi)}{\overline{EI}}\,r\,\sin(\varphi)\underbrace{-E(r,\varphi)\Big[\alpha_T(r,\varphi)\Delta T(r) - \varepsilon_0^e\Big]}_{\sigma_w^e(r,\varphi)}. \qquad \text{(B.28)}\end{aligned}$$

Thus, the self-equilibrated stresses resulting from prevented eigenwarping of the cross-section of a cylindrical reinforced concrete column read as

$$\sigma_w^e(r,\varphi) = -E(r,\varphi)\Big[\alpha_T(r,\varphi)\Delta T(r) - \varepsilon_0^e\Big]\,. \qquad \text{(B.29)}$$

The expression in the square brackets of Eq. (B.29) is equal to the nonlinear part of the eigenstrains, ε_w^e, see Eq. (B.25). In the case of uniform heating at the lateral surface of the column as described in Appendix A and under consideration of the definition of temperature changes ΔT, the self-

equilibrated stresses resulting from prevented eigenwarping of the cross-section of a cylindrical reinforced concrete column read as

$$\begin{aligned}\sigma_w^e(r,\varphi) = E(r,\varphi)\Bigg[&\Delta T^{lat}\left(\alpha_T(r,\varphi) - \frac{A_c}{A_{tr}}\alpha_{T,c}\right)\\ &+ \sum_{k=1}^{N_T}\frac{4(T_{ref}-\Delta T_k^{lat})}{R^2}\sum_{n=1}^{\infty}\frac{1}{\lambda_n}\left(\frac{R}{2}\frac{J_0(\lambda_n r)}{J_1(\lambda_n R)}\alpha_T(r,\varphi) - \frac{A_c}{A_{tr}}\frac{\alpha_{T,c}}{\lambda_n}\right)\exp(-\lambda_n^2 a\langle t-t_k\rangle)\\ &- n_E\,\alpha_{T,s}\sum_{j=1}^{L}\frac{A_{s,j}}{A_{tr}}\Delta T_j\Bigg]. \end{aligned} \tag{B.30}$$

Specializing Eq. (B.28) for concrete stresses, under consideration of the modulus of elasticity $E(r,\varphi) = E_c$, the thermal expansion coefficient $\alpha_T(r,\varphi) = \alpha_{T,c}$, and Eqs. (B.13) and (B.22), leads to

$$\sigma_{xx,c}(r,\varphi) \quad = \quad \frac{N}{A_{tr}} + \frac{M}{I_{tr}}\,r\,\sin(\varphi) - \underbrace{E_c\Big[\alpha_{T,c}\,\Delta T(r) - \varepsilon_0^e\Big]}_{\sigma_w^e(r)}, \tag{B.31}$$

and

$$\begin{aligned}\sigma_w^e(r) = E_c\Bigg[&\alpha_{T,c}\,\Delta T^{lat}\left(1 - \frac{A_c}{A_{tr}}\right)\\ &+ \sum_{k=1}^{N_T}\frac{4(T_{ref}-\Delta T_k^{lat})}{R^2}\sum_{n=1}^{\infty}\frac{1}{\lambda_n}\left(\frac{R}{2}\frac{J_0(\lambda_n r)}{J_1(\lambda_n R)} - \frac{A_c}{A_{tr}}\frac{1}{\lambda_n}\right)\exp(-\lambda_n^2 a\langle t-t_k\rangle)\\ &- n_E\,\alpha_{T,s}\sum_{j=1}^{L}\frac{A_{s,j}}{A_{tr}}\Delta T_j\Bigg]. \end{aligned} \tag{B.32}$$

Appendix C

List of Symbols

symbol	meaning
A	total area of the cross-section
A_c	concrete area
A_s	total reinforcement/steel area
$A_{s,j}$	area of one reinforcement bar
A_{tr}	area of the transformed cross-section
a	thermal diffusivity
$\alpha_T(x,y), \alpha_T(r,\varphi)$	non-uniform thermal expansion coefficient
$\alpha_{T,c}$	thermal expansion coefficient of concrete
$\alpha_{T,s}$	thermal expansion coefficient of reinforcement/steel
b	width of the beam
c	specific heat capacity
ΔT_j	temperature change of the j^{th} reinforcement bar
ΔT_k	k^{th} temperature step at the surface
ΔT_k^{top}, ΔT_k^{bot}	k^{th} temperature step at the top and bottom surface of the beam
ΔT_k^{lat}	k^{th} temperature step at the lateral surface of the column
$\Delta T(z,t)$	temperature change in Cartesian coordinates, measured relative to T_{ref}
$E(x,y)$, $E(r,\varphi)$	non-uniform modulus of elasticity
E_c	modulus of elasticity of concrete
E_s	modulus of elasticity of reinforcement/steel
$\overline{EA}$	effective extensional stiffness
$\overline{EI}$	effective bending stiffness
ε_{xx}	axial strain component in x-direction
ε^e_{xx}, ε^e_{yy}, ε^e_{zz}	eigenstrains in x-, y and z-direction (Cartesian coordinates)
ε^e_{xx}, ε^e_{rr}, $\varepsilon^e_{\varphi\varphi}$	eigenstrains in x-, r and φ-direction (cylindrical coordinates)
ε_0	stretch of the beam axis
ε^e_0	thermal eigenstretch of the beam axis
ε^e_w	thermal eigenwarping of the cross-section of the beam
η_A, η_I	ratio factors
h	height of the beam
$\boldsymbol{I}$	second order identity tensor
I	second moment of inertia of a homogeneous cross-section
I_c	second moment of inertia of concrete part of the cross-section
I_{tr}	second moment of inertia of the transformed cross-section
$J_\nu()$	ν^{th} order Bessel function of the first kind
$\boldsymbol{K}$	second order tensor of thermal conductivity
κ_0	curvature of the beam axis
κ^e_0	thermal eigencurvature of the beam axis

symbol	meaning
L	number of reinforcement bars of the cross-section
ℓ	length of the structural elements
λ_n	eigenvalues of the spatially part of the solution of radial heat conduction
M	bending moment
N	axial force
N_T	number of temperature steps
n_E	ratio between the modulus of elasticity of steel and concrete
∇	nabla operator
P_1, P_2, P_3	point loads
R	radius of the column
ρ	mass density
σ_{xx}	axial stress component of Cauchy's tensor in x-direction
$\sigma_{xx,m}$	axial stresses in x-direction resulting from mechanical loading
$\sigma_{xx,tot}$	total axial stresses in x-direction resulting from mechanical and thermal loading
σ_w^e	axial stresses resulting from prevented eigenwarping of the cross-section
$T^{bot}(t)$	temperature history at the bottom surface of the beam
$T^{lat}(t)$	temperature history at the lateral surface of the column
$T(r,t)$	temperature variable in cylindrical coordinates
$T(z,t)$	temperature variable in Cartesian coordinates
T_k	surface temperature at at the k^{th} step
T_{ref}	reference temperature
t	time variable
t_k	simulation time at at the k^{th} temperature step
$\langle t - t_k \rangle$	Macauley operator
u, w	displacement components in x-, and z-direction
x, r, φ	cylindrical coordinates
x, y, z	Cartesian coordinates
$Y_\nu()$	ν^{th} order Bessel function of the second kind
$z_{s,j}$	location of the j^{th} reinforcement bar, measured from the beam axis
z_n	normalized coordinates in z-direction

Bibliography

[1] S. Albrifkani and Y. C. Wang. “Explicit modelling of large deflection behaviour of restrained reinforced concrete beams in fire”. In: *Engineering Structures* 121 (2016), pp. 97–119.

[2] M. Ausweger. “Spannungen und Verformungen gerader Einzelstäbe zufolge Temperaturbeanspruchung”. Bachelorarbeit. Technische Universität Wien, 2016.

[3] S. Bratina, B. Cas, M. Saje, and I. Planinc. “Numerical modelling of behaviour of reinforced concrete columns in fire and comparison with Eurocode 2”. In: *Solids and Structures* 42 (2005), pp. 5715–5733.

[4] E. Choi and Y. Shin. “The structural behavior and simplified thermal analysis of normal-strength and high-strength concrete beams under fire”. In: *Engineering Structures* 33 (2011), pp. 1123–1132.

[5] P.-H. Chuang and S.-K. Kong. “Strength of Slender Reinforced Concrete Columns”. In: *Journal of structural engineering* 124(9) (1998), pp. 992–998.

[6] Dassault Systemes Simulia Corp. *ABAQUS CAE*. 2019.

[7] R. Diaz, H. Wang, H. Mang, Y. Yuan, and B. Pichler. “Numerical Analysis of a Moderate Fire inside a Segment of a Subway Station”. In: *applied sciences* 8 (2018), pp. 1–34.

[8] Dlubal Software GmbH. *RStab*. Version 8.22. 2020.

[9] M. Dwaikat and V. Kodur. “A numerical approach for modeling the fire induced restraint effects in reinforced concrete beams”. In: *Fire Safety* 43 (2008), pp. 291–307.

[10] S. El-Fitiany and M. Youssef. “A simplified sectional analysis approach for RC elements during fire events”. In: *Structures in Fire* (2010), pp. 239–246.

[11] S. El-Fitiany and M. Youssef. “Fire performance of reinforced concrete frames using sectional analysis”. In: *Engineering Structures* 142 (2017), pp. 165–181.

[12] S. El-Fitiany and M. Youssef. “Interaction diagrams for fire-exposed reinforced concrete sections”. In: *Engineering Structures* 70 (2014), pp. 246–259.

[13] S. El-Fitiany and M. Youssef. “Simplified method to analyze continuous reinforced concrete beams during fire exposure”. In: *ACI Structural Journal* 111 (2014), pp. 145–155.

[14] J.-M. Franssen and J.-C. Dotreppe. “Fire Tests and Calculation Methods for Circular Concrete Columns”. In: *Fire Technology* 39 (2003), pp. 89–97.

[15] W. Gao, J.-G. Dai, J. Teng, and G. Chen. “Finite element modeling of reinforced concrete beams exposed to fire”. In: *Engineering Structures* 52 (2013), pp. 488–501.

[16] N. Hannoschöck. *Wärmeleitung und -transport - Grundlagen der Wärme und Stoffübertragung*. Berlin: Springer, 2018.

[17] T. Hasenbichler. “Semi-analytische Berechnung von Wärmespannungen in Stäben”. Bachelorarbeit. Technische Universität Wien, 2019.

[18] C. Hellmich, R. Höller, J. Kalliauer, O. Lahayne, B. Pichler, L. Pircher, R. Plachy, and V. Wittner. “Skriptum zur Vorlesung mit Übung aus Ingenieurmechanik”. In: (2019), pp. 3–6.

[19] P. Kamath, U. Kumar Sharma, V. Kumar, P. Bhargava, A. Usmani, B. Singh, Y. Singh, J. Torero, M. Gillie, and P. Pankaj. "Full-scale fire test on an earthquake-damaged reinforced concrete frame". In: *Fire Safety Journal* 73 (2015), pp. 1–19.

[20] V. Kodur and M. Dwaikat. "A numerical model for predicting the fire resistance of reinforced concrete beams". In: *Cement & Concrete Composites* 30 (2008), pp. 431–443.

[21] L. Lu, J. Qiu, Y. Yuan, J. Tao, H. Yu, H. Wang, and H. Mang. "Large-scale test as the basis of investigating the fire-resistance of underground RC substructures". In: *Engineering Structures* 178 (2018), pp. 12–23.

[22] J. Ozbolt, J. Bošnjak, G. Periškic, and A. Sharma. "3D numerical analysis of reinforced concrete beams exposed to elevated temperature". In: *Engineering Structures* 58 (2014), pp. 166–174.

[23] T. Ring, M. Zeiml, and R. Lackner. "Underground concrete frame structures subjected to fire loading: Part I – Large-scale fire tests". In: *Engineering Structures* 58 (2014), pp. 175–187.

[24] T. Ring, M. Zeiml, and R. Lackner. "Underground concrete frame structures subjected to fire loading: Part II – Re-analysis of large-scale fire tests". In: *Engineering Structures* 58 (2014), pp. 188–196.

[25] S. Schmid. "Stresses in a concrete pavement resulting from transient heat conduction: engineering analysis of in situ temperature measurements". Diplomarbeit. Technische Universität Wien, 2020.

[26] R. Sun, B. Xie, R. Perera, and Y. Pan. "Modeling of Reinforced Concrete Beams Exposed to Fire by Using a Spectral Approach". In: *Advances in Materials Science and Engineering* (2018), pp. 1–12.

[27] E. H. El-Tayeb, S. E. El-Metwally, H. S. Askar, and A. M. Yousef. "Thermal analysis of reinforced concrete beams and frames". In: *HBRC Journal* 13 (2017), pp. 8–24.

[28] A. Tayem and A. Najmf. "Design of Round Reinforced-Concrete Columns". In: *Journal of structural engineering* 122(9) (1996), pp. 1062–1071.

[29] F. J. Vecchio. "Nonlinear Analysis of Reinforced Concrete Frames Subjected". In: *ACI Structural Journal* 84 (1987), pp. 492–501.

[30] F. J. Vecchio and J. A. Sato. "Thermal gradient effects in reinforced concrete frame structures". In: *ACI Structural Journal* 87 (1990), pp. 262–275.

[31] H. Wang, R. Höller, M. Aminbaghai, C. Hellmich, Y. Yuan, H. A. Mang, and B. L. A. Pichler. "Concrete pavements subjected to hail showers: A semi-analytical thermoelastic multiscale analysis". In: *Engineering Structures* 200 (2019), pp. 1–19.

[32] X. Zha. "Three-dimensional non-linear analysis of reinforced concrete members in fire". In: *Building and Environment* 38 (2003), pp. 297–307.